

Fast logic with slow qubits: microwave-activated controlled-Z gate on low-frequency fluxoniums

Quentin Ficheux,^{1,*} Long B. Nguyen,^{1,*} Aaron Somoroff,¹ Haonan Xiong,¹
Konstantin N. Nesterov,² Maxim G. Vavilov,² and Vladimir E. Manucharyan¹

¹*Department of Physics, Joint Quantum Institute,
and Center for Nanophysics and Advanced Materials,
University of Maryland, College Park, MD 20742, USA*

²*Department of Physics and Wisconsin Quantum Institute,
University of Wisconsin - Madison, Madison, WI 53706, USA*

(Dated: November 6, 2020)

We demonstrate a controlled-Z gate between capacitively coupled fluxonium qubits with transition frequencies 72.3 MHz and 136.3 MHz. The gate is activated by a 61.6 ns long pulse at the frequency between non-computational transitions $|10\rangle - |20\rangle$ and $|11\rangle - |21\rangle$, during which the qubits complete only 4 and 8 Larmor periods, respectively. The measured gate error of $(8 \pm 1) \times 10^{-3}$ is limited by decoherence in the non-computational subspace, which will likely improve in the next generation devices. Although our qubits are about fifty times slower than transmons, the two-qubit gate is faster than microwave-activated gates on transmons, and the gate error is on par with the lowest reported. Architectural advantages of low-frequency fluxoniums include long qubit coherence time, weak hybridization in the computational subspace, suppressed residual ZZ -coupling rate (here 46 kHz), and absence of either excessive parameter matching or complex pulse shaping requirements.

I. INTRODUCTION

Macroscopic superconducting circuits have emerged as a leading platform for implementing a quantum computer [1]. Currently available small-scale superconducting quantum processors [2–9] have achieved a number of important milestones, including the break-even point in quantum error correction of a single logical qubit [10], digital quantum simulation [11–16], non-trivial optimization algorithms [17–19], and, an example demonstration of quantum supremacy with 53 qubits [20]. This progress is even more spectacular as it is solely based on a single qubit type, the transmon, which is essentially a weakly-anharmonic electromagnetic oscillator [21]. Although the transmon’s simplicity makes it an exceptionally robust quantum system, its relatively weak non-linearity has become a major limiting factor for current performance and further scaling of quantum processors. Irrespective of implementation details, a weak anharmonicity inevitably leads to slower two-qubit gates, which makes them prone to decoherence errors. Therefore, a motivation has built up for exploring strongly-anharmonic alternatives to transmons that would ideally have higher intrinsic coherence and be compatible with the transmon-based scaling architectures.

In recent years, long coherence times (up to $T_2 = 500 \mu s$) were repeatedly observed in superconducting fluxonium qubits [22, 23]. In this paper we describe the first logical operation on a pair of capacitively-coupled fluxoniums [Fig. 1(a)]. Each fluxonium has one weak Josephson junction and a large capacitor, which are the

same components as in the transmon, but the junction is additionally shunted by a large-value inductance [24], made from a chain of about 100 stronger junctions. Inductive shunting makes the charges on the fluxonium capacitors continuous, and hence, contrary to transmons, fluxoniums can have highly anharmonic spectra insensitive to offset charges. We operate fluxoniums near the half-integer flux bias (“sweet spot”), where the qubit transition frequency is first order insensitive to flux noise and belongs to a 100 – 1000 MHz range. The order of magnitude qubit slowdown, compared to typically 5 – 6 GHz transmons, dramatically reduces the rate of energy relaxation due to dielectric loss, an important decoherence mechanism in superconducting circuits. This straightforward trick proved largely responsible for the long coherence time of fluxoniums [22]. However, how can one slow qubits down without ending up with slower two-qubit gates?

To answer this general question, we consider the simplest form of circuit-circuit coupling by means of a mutual capacitance. In analogy with transmons, we get a coupling term proportional to $n_A n_B$, where n_A and n_B are the charge operators of qubits A and B, normalized to the Cooper pair charge $2e$. First, we notice that capacitive coupling indeed produces little effect on the computational states $|00\rangle$, $|01\rangle$, $|10\rangle$, $|11\rangle$, because the transition matrix elements of $n_{A(B)}$ vanish with the transition frequency. For the same reason, the much higher energy non-computational states $|12\rangle$ and $|21\rangle$ can experience a noticeable repulsion, while the only nearby states $|20\rangle$ and $|02\rangle$ remain unaffected due to the parity selection rule, see Fig. 1(b). Therefore, connecting the two subspaces with radiation can induce an on-demand qubit-qubit interaction. For example, Ref. [25] describes a controlled-Z (CZ) gate obtained by applying a 2π -

* Equal contribution author

pulse to transition $|11\rangle - |21\rangle$ while the closest transition $|10\rangle - |20\rangle$ stays unexcited. This condition can always be met if the gate pulse is much longer than $1/\Delta$, where Δ is the shift of level $|21\rangle$ due to the $n_A n_B$ -term, shown in Fig. 1(b). Yet, we show that with an optimal combination of drive detuning and amplitude, the CZ-gate can be completed in a time close to $1/\Delta$ with zero leakage outside the computational subspace, thanks to synchronization of Rabi rotations of both non-computational transitions. For our specific device parameters (see Tables I, II), we get $\Delta = 22$ MHz ($1/\Delta = 45.5$ ns) and the optimal gate time is 61.6 ns. Remarkably, since Δ is not tied to the qubit frequencies (here 72.3 MHz and 136.3 MHz), the logical operation takes just a few qubit Larmor periods. To our knowledge, such a high relative gate speed is unmatched across quantum computing platforms.

Population transit through non-computational states is common in gates realized with transmons [26–33]. For example, repulsion of states $|11\rangle$ and $|20\rangle$ enables a CZ-gate via flux-tuning of these states in and out of resonance [27]. Recent high-fidelity versions of this gate rely on diabatic flux pulses [30, 33], resulting in a significant population of state $|20\rangle$ for a short time, which draws parallels to our microwave-controlled scheme. In the case of fixed-frequency qubits, repulsion between states $|30\rangle$ and $|21\rangle$ was used in Ref. [34] to implement a CZ-gate activated by a microwave pulse at a frequency near the transition $|11\rangle - |12\rangle$. However, the insufficient transmon anharmonicity introduces many nearby transitions (there is only one relevant transition $|10\rangle - |20\rangle$ for fluxoniums), and in the end such a gate proved impractical. Even in gates designed to operate entirely within the computational subspace, e.g. the flux-activated $|10\rangle - |01\rangle$ swap gate [35–37] or the cross-resonance gate [38, 39], uncontrolled population leakage to non-computational states remains an important factor limiting gate speed [40]. Yet, such coherent errors can be practically eliminated in fluxoniums owing to their highly anharmonic spectra, as exemplified by the gate scheme reported here.

Another important advantage of fluxoniums over fixed-coupling transmons is that the static ZZ -shift, coming from the repulsion of computational and non-computational states, can be suppressed by over an order of magnitude compared to typical values in capacitively coupled transmons (here about 40 kHz), largely thanks to the low qubit frequencies. For transmons, the static ZZ -shift is an important source of gate error, the mitigation of which draws additional resources. Thus, in the case of the cross-resonance gate, the ZZ -term is suppressed by a combination of circuit parameter matching, additional echo pulse sequences incorporated into the gate protocol [40], and additional qubit rotations [41]. An alternative strategy to eliminate the ZZ -shift is to use flux-tunable couplers [20, 42, 43], which in practice act as separate quantum systems and hence increase the circuit complexity. More recently, the ZZ -shift was suppressed in capacitively-shunted flux qubits using an additional drive, but at the expense of operating away from the flux

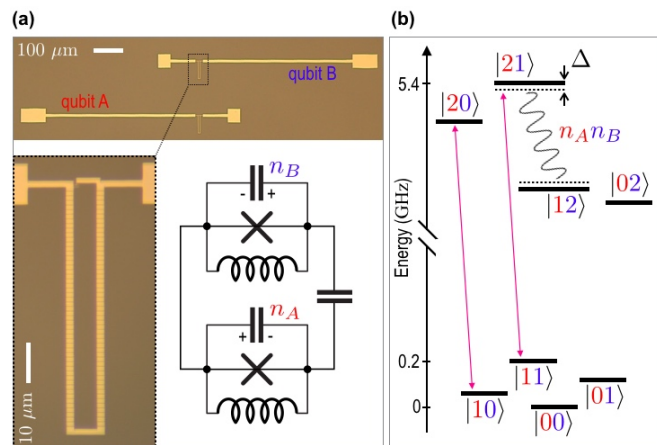


FIG. 1. (a) Optical image of two capacitively-coupled fluxoniums fabricated on a silicon chip along with their minimal circuit model. Devices are similar to those reported in Ref. [22] except the antennas are intentionally made asymmetric for optimal coupling to the readout cavity [not shown]. (b) Diagram of the lowest energy states of the interacting two-fluxonium system. Capacitive coupling induces a shift of level $|21\rangle$ by Δ due to repulsion from level $|12\rangle$. The shift Δ leads to a CZ-operation in time approximately given by $1/\Delta$ when either qubit is driven at a frequency in between the transitions $|10\rangle - |20\rangle$ and $|11\rangle - |21\rangle$.

sweet-spot [44].

The gate error in our scheme is largely limited by decoherence outside the computational subspace. Randomized benchmarking yields the averaged gate error of 8×10^{-3} , which is consistent with the measured few microsecond coherence time of transitions $|10\rangle - |20\rangle$ and $|11\rangle - |21\rangle$ (see Table II). Because these transitions are transmon-like, we expect their coherence will improve by an order of magnitude in the next generation experiments with improved fabrication and noise filtering procedures. This step would lower the gate error into the 10^{-4} -range. The presently achieved fidelity is on par with the lowest reported values in microwave-activated gates [41, 45] (cross-resonance gate by IBM). Additionally, our gate is considerably faster than cross-resonance type gates with comparable errors [40, 46]. Our result illustrates the potential of highly-anharmonic circuits for quantum information processing and it motivates the exploration of large-scale quantum processors based on fluxoniums.

The paper is organized as follows, in Sec. II we describe the details of our experimental setup, including spectroscopy of the two-fluxonium device, the joint single-shot readout of fluxoniums, and state initialization procedures. In Sec. III we detail the concepts behind our fast microwave-activated CZ-gate. Section IV presents the results of gate characterization, including quantum process tomography and randomized benchmarking. In Sec. V we review the technical limitations of the present experiment, and project the near term improvements. Section VI concludes the work.

II. TWO-FLUXONIUM SYSTEM CHARACTERIZATION

Our device is composed of two fluxonium artificial atoms with a circuit design introduced in [22] coupled via a shared capacitance [see Fig. 1(a)]. The system obeys the Hamiltonian [25, 47]

$$\frac{\hat{H}}{\hbar} = \sum_{\alpha=A,B} 4E_{C,\alpha} \hat{n}_\alpha^2 + \frac{1}{2} E_{L,\alpha} \hat{\varphi}_\alpha^2 - E_{J,\alpha} \cos(\hat{\varphi}_\alpha - \phi_{\text{ext},\alpha}) + J_C \hat{n}_A \hat{n}_B \quad (1)$$

where $E_{C,\alpha}$, $E_{L,\alpha}$, and $E_{J,\alpha}$ are the charging energy, the inductive energy and the Josephson energy of fluxonium indexed by $\alpha = A, B$, respectively. The operators $\hat{\varphi}_\alpha$ and \hat{n}_α are the phase twist across the inductance L_α and the charge on the capacitor C_α , and they commute according to $[\hat{\varphi}_\alpha, \hat{n}_\alpha] = i$. The experimentally extracted parameters of the Hamiltonian (1) are given in Table I.

	$E_{C,\alpha}$ (GHz)	$E_{L,\alpha}$ (GHz)	$E_{J,\alpha}$ (GHz)	J_C (GHz)
Qubit A	0.973	0.457	5.899	0.224
Qubit B	1.027	0.684	5.768	

TABLE I. Parameters of Hamiltonian Eq. (1) extracted by its fitting to the two-tone spectroscopy data in Fig. 2.

When biased at $\phi_{\text{ext},\alpha} = \pi$, the fluxoniums are at their sweet spots with respect to external flux. The qubit frequencies $f_A = 72.3$ MHz and $f_B = 136.3$ MHz are almost two orders of magnitude lower than the typical transition frequency in cavity resonators and transmon qubits [48]. These low frequency transitions exhibit a long energy relaxation times $T_{1,A} = 347$ μ s and $T_{1,B} = 282$ μ s owing to their decoupling from dielectric loss mechanisms [22]. A slight non-uniformity in the magnetic field, provided by a single external coil, prevents biasing qubits precisely at their sweet-spots simultaneously, with the offset being about 0.14% of the flux quantum. We operate at a bias coil current of 33.7 μ A, approximately halfway between the two sweet spots, which reduced the spin echo coherence times to $T_{2,A}^E = 31$ μ s and $T_{2,B}^E = 64$ μ s (see Table II) compared to their sweet spot values of 47 μ s and 67 μ s, respectively. The sweet-spot values of coherence times are likely limited by photon shot-noise due to imperfect thermalization of the readout cavity [49]. This common issue can be improved with better filtering of the measurement lines. We note in advance that the small deviation from the sweet-spots does not modify appreciably the operation of our two-qubit gates, and the qubit coherence times are not limiting the gate error.

Higher energy states are separated from the computational states by an approximately 4.5 GHz gap (Fig. 2 - top panel). The capacitive coupling term $J_C \hat{n}_A \hat{n}_B$ in Eq. (1) with $J_C = 224$ MHz manifests itself in the spectrum of lowest non-computational transitions. Mainly,

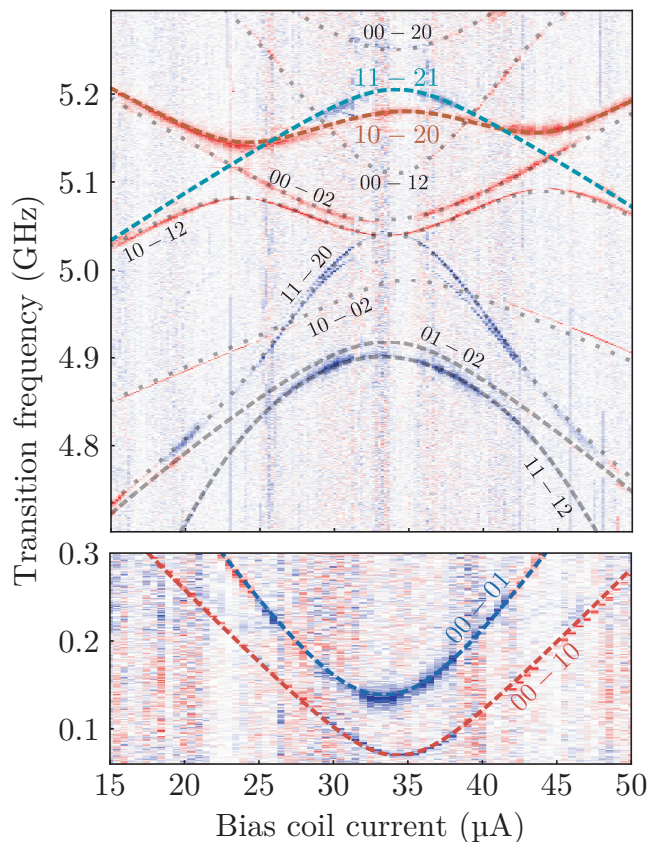


FIG. 2. Two-tone spectroscopy as a function of probe tone frequency and flux threading the common biasing coil. The parameters of the system (Table I) are extracted by fitting the spectroscopy data to the diagonalization of the Hamiltonian (1). Dashed lines represent transitions allowed at half-integer flux while dotted lines represent transitions that are forbidden at sweet spot. The shared capacitance lifts the degeneracy between the two $|11\rangle - |21\rangle$ and $|10\rangle - |20\rangle$ transitions by an amount Δ (top panel) that limits the gate speed. The sweet spots misalignment (bottom panel) is attributed to a local flux imbalance through the two fluxonium loops $\phi_{\text{ext},A} \neq \phi_{\text{ext},B}$.

the interaction creates a frequency splitting between transitions $|10\rangle - |20\rangle$ and $|11\rangle - |21\rangle$ of $\Delta = 22$ MHz. Note that the extracted value of J_C corresponds to the mutual capacitance between the qubit circuits of about 1.2 fF, which is comparable to the typical mutual capacitance used for coupling transmons in quantum processors. Owing to the matrix element hierarchy $n_{i-1}^\alpha \ll n_{i-2}^\alpha$, where $n_{i-j}^\alpha = |\langle i | \hat{n}_\alpha | j \rangle|$ is the charge matrix element of fluxonium α , the transverse interaction in the computational subspace is negligible. Interaction involving higher levels also introduces a static longitudinal ZZ -interaction in the computational subspace [42, 44] given by $\xi_{ZZ} = (E_{00} + E_{11} - E_{01} - E_{10})/\hbar = 46$ kHz, where E_{ij} is the energy of state $|ij\rangle$. We note that this value of ξ_{ZZ} is at least an order of magnitude smaller than in typical transmon circuits and does not require extra spectroscopy optimizations beyond having low qubit-transitions

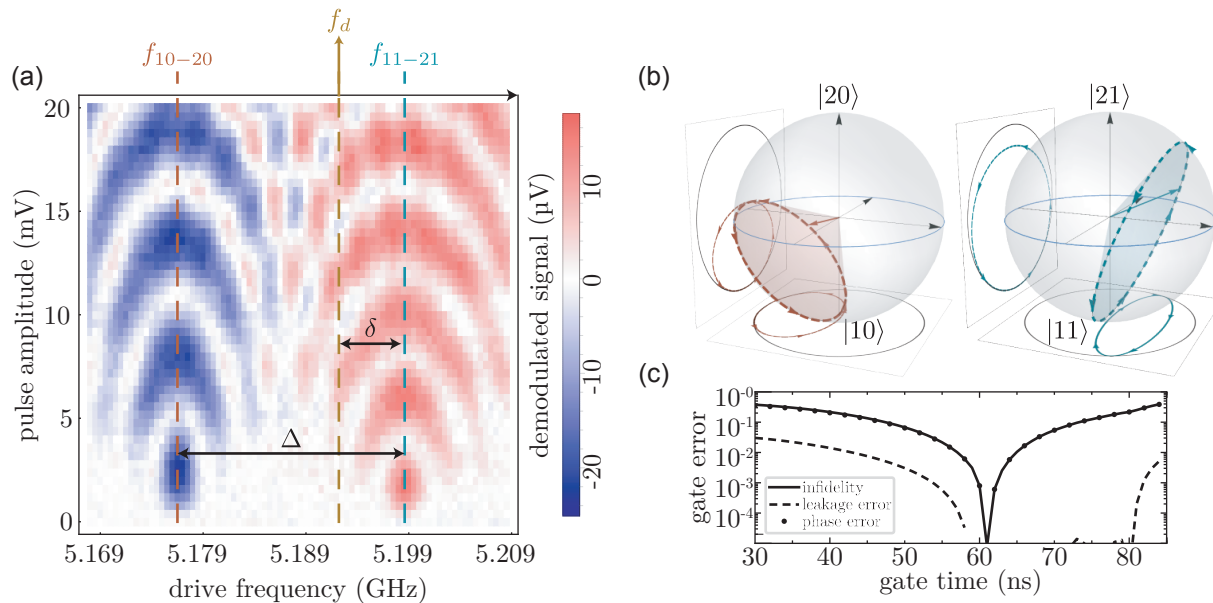


FIG. 3. Gate principle. (a) Rabi oscillations near the $|10\rangle - |20\rangle$ and $|11\rangle - |21\rangle$ transitions versus driving frequency with a 330 ns-long pulse. The two transitions display different resonance Rabi frequencies characterized by the ratio $r = \Omega_{11-21}/\Omega_{10-20} \simeq 1.36$. The drive frequency f_d indicated in brown given by Eq. (4) is used to synchronize the oscillations on the two transitions. (b) Bloch sphere representations of the trajectories in the $\{|10\rangle, |20\rangle\}$ and $\{|11\rangle, |21\rangle\}$ manifolds in the frame rotating at the drive frequency. The quantum state follows a closed path in the Hilbert space leading to a relative phase accumulation given by the difference of the solid angles spanned by the two trajectories. (c) Gate error versus gate duration simulated using the Hamiltonian given by Eq. (1) in the presence of a Gaussian flat-topped pulse and without decoherence. For every gate duration, drive frequency and amplitude are optimized to minimize the coherent leakage error (dashed line). The dots represent the gate error caused by incorrect phase accumulation $\Delta\varphi = \varphi_{11} - \varphi_{10} \neq \pi$. With the optimal pulse duration around ~ 62 ns, the infidelity due to coherent errors is well below 10^{-3} .

frequencies.

The device is embedded in a 3-dimensional copper cavity with a resonant frequency of $f_c = 7.4806$ GHz. Prior to each experiment, the qubits are initialized by applying a strong microwave pulse on the cavity (see Appendix C3). This procedure increases the excited state probability of the qubits to 86% and 88% which is sufficient for metrology of gate operations. The remaining qubit entropy corresponds to temperatures of $T_A = 3.7$ mK and $T_B = 5.9$ mK well below the fridge temperature of 14 mK. We achieve a single-shot joint readout of the two qubits by sending a cavity tone of optimal frequency, power, and duration. The outgoing signal is further amplified by a Josephson Traveling Wave Parametric Amplifier (JTWPA) [50] and commercial amplifiers before down-conversion and numerical demodulation. We finally correct for readout imperfections by a procedure described in Appendix C2.

III. FAST CZ-GATE BY EXACT LEAKAGE CANCELLATION

In this section, we describe how to exploit the fluxonium interaction to implement a CZ gate in the shortest possible time. Let us start by considering the gate

transitions $|10\rangle - |20\rangle$ and $|11\rangle - |21\rangle$ as two-level systems. Our gate exploits the geometric-phase accumulations during round trips in these two systems. The accumulated phase can be divided into two parts: the dynamical phase, which is proportional to the evolution time and the energy of the system, and the geometric phase, which depends only on the trajectory followed in the Hilbert space. Applying a microwave tone drives the system with the Hamiltonian

$$\frac{\hat{H}_{\text{drive}}}{h} = (\epsilon_A \hat{n}_A + \epsilon_B \hat{n}_B) \cos(2\pi f_d t). \quad (2)$$

When the drive frequency f_d is nearly resonant with the gate transitions, we observe Rabi oscillations [Fig. 3(a)] with the resonance Rabi frequencies $\Omega_{10-20} = |\langle 10 | \hat{H}_{\text{drive}} | 20 \rangle|/h$ and $\Omega_{11-21} = |\langle 11 | \hat{H}_{\text{drive}} | 21 \rangle|/h$, respectively. A strong hybridization of the $|12\rangle$ and $|21\rangle$ states creates an imbalance between the rotation speeds given by the ratio $r = \Omega_{11-21}/\Omega_{10-20} \simeq 1.36$.

In order to eliminate leakage to higher states, one needs to synchronize off-resonance Rabi oscillations determined by the two transitions to ensure that the state vector always comes back to the computational subspace. This is achieved by matching the generalized Rabi frequencies

$$\Omega = \sqrt{\Omega_{11-21}^2 + \delta^2} = \sqrt{\Omega_{10-20}^2 + (\delta - \Delta)^2}, \quad (3)$$

where $\delta = f_{11-21} - f_d$ is the detuning between the $|11\rangle - |21\rangle$ transition and the drive frequency [Fig. 3(a)]. A full rotation is then preformed in the shortest gate time $t_{\text{gate}} = 1/\Omega$. During the gate operation, the state vector trajectory can be depicted in a Bloch sphere representation [Fig. 3(b)] when the system starts in $|10\rangle$ or $|11\rangle$. These circular trajectories, which are traveled in opposite directions with respect to the centers of the Bloch spheres, define two cones inside the spheres. The cones and directions of travel define the solid angles $\Theta_{10} = 2\pi[1 - (\Delta - \delta)/\Omega]$ and $\Theta_{11} = 2\pi(1 + \delta/\Omega)$, which correspond to a geometric phase accumulation $\varphi_{ij} = -\Theta_{ij}/2$ on state $|ij\rangle$. Our gate thus implements a unitary operation $U = \text{diag}(1, 1, e^{i\varphi_{10}}, e^{i\varphi_{11}})$. Using virtual Z rotations [51], the phase difference can be assigned to any computational state such as $|11\rangle$ to realize a controlled-Phase operation $U = \text{diag}(1, 1, 1, e^{i\Delta\varphi})$ with $\Delta\varphi = \varphi_{11} - \varphi_{10}$. A CZ gate is obtained when $\Delta\varphi = -(\Theta_{11} - \Theta_{10})/2 = -\pi\Delta/\Omega = \pm\pi$. Using this condition in Eq. (3) we obtain the optimal drive frequency [brown arrow on Fig. 3(a)]

$$\frac{\delta}{\Delta} = \frac{r^2 - \sqrt{(r^2 - 1)^2 + r^2}}{r^2 - 1} \simeq 0.29. \quad (4)$$

For δ given by Eq. (4) and $\Omega = \Delta$, a CZ gate with zero leakage is achieved in time exactly $t_{\text{gate}} = 1/\Delta$.

Our understanding of the gate process is validated by simulating the full Hamiltonian Eq. (1) in the presence of the drive Hamiltonian, Eq. (2). The full Hamiltonian takes into account the dynamical phase $\phi_{\text{dyn}} = 2\pi\xi_{ZZ}t_{\text{gate}} \simeq 10^{-2} \ll \pi$ which is negligible after one gate operation thanks to the small ZZ-interaction term. Starting with the driving frequency given by Eq. (4), we minimize the final populations leakage out of the computational subspace by adjusting the drive amplitude and frequency for every gate duration. Because of the rising and lowering edges of the pulse in the simulation, we find a slightly longer optimal gate duration ~ 61 ns (compared to $1/\Delta = 45.5$ ns) for which coherent errors on the gate fall below $< 10^{-3}$, see Fig. 3(c). Note, even at the error level of 10^{-4} , the optimal point does not require an excessive fine-tuning of the gate pulse parameters: it corresponds to a fraction of a percent variation in terms of the gate time, gate pulse amplitude, and frequency (see Appendix F). Our procedure can readily be extended to any other phase accumulation by imposing a different phase-accumulation condition leading to a different gate duration and modified single-qubit virtual Z rotations.

IV. GATE CALIBRATION AND METROLOGY

Using our understanding from the previous section, we start with the following initial gate parameters: we use a 60 ns flat-top Gaussian pulse with a driving amplitude corresponding to a full rotation at the gate frequency given by Eq. (4). To measure the accumulated phase

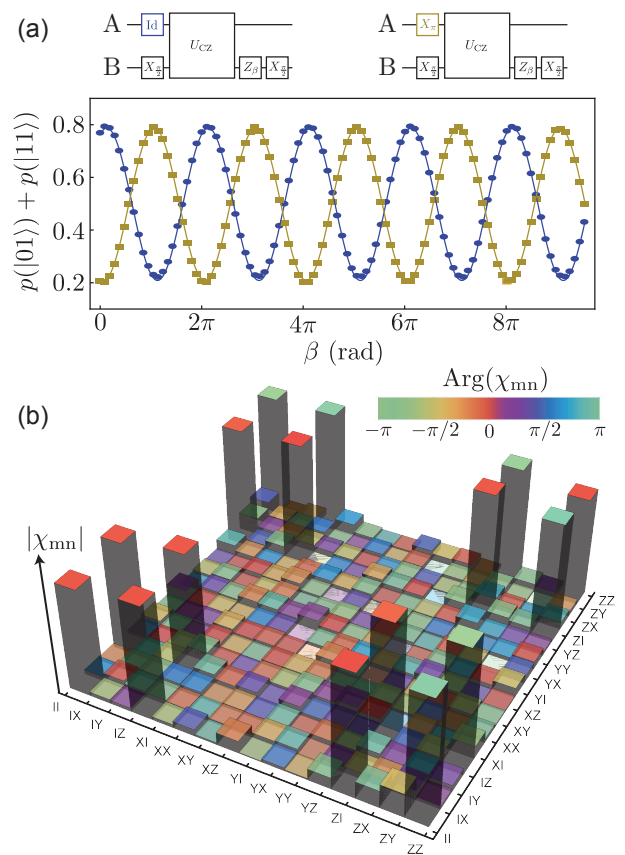


FIG. 4. Controlled-Z gate. (a) Pulse sequences of a Ramsey-type experiment measuring the phase of qubit B after a CZ operation. Ramsey fringes are obtained by varying the rotation angle β . The excited state population of qubit B $p_1^B = p(|01\rangle) + p(|11\rangle)$ oscillates with β with a phase that depends on the state of the control qubit A. The blue and brown fringes are obtained by flipping the state of qubit A at the beginning of the sequence revealing the conditional phase accumulated during the gate $\Delta\varphi \simeq 0.95\pi$. (b) Quantum process tomography of the CZ gate. The experimentally extracted process tomography matrix χ reproduces a CZ operation with a fidelity of 0.97.

difference $\Delta\varphi$, we perform a Ramsey-type experiment on qubit B to compare the phases of the superpositions $|11\rangle + |10\rangle$ and $|01\rangle + |00\rangle$ after the application of a CZ gate. This is achieved by inserting a CZ gate between two successive $\pi/2$ pulses with a relative phase β created by a virtual Z rotation [51]. When the angle β is varied, we observe Ramsey fringes with an initial phase encoding the excited state probability of the control qubit A. The phase difference when qubit A is prepared in the ground or excited state yield the relative phase accumulation $\Delta\varphi/\pi \simeq 0.95$ [in Fig. 4(a)] close to the phase required for the CZ gate.

In order to gain more insight in the physics of our gate, we perform quantum process tomography by preparing 16 independent input states, applying the CZ gate to each of them before performing their state tomography.

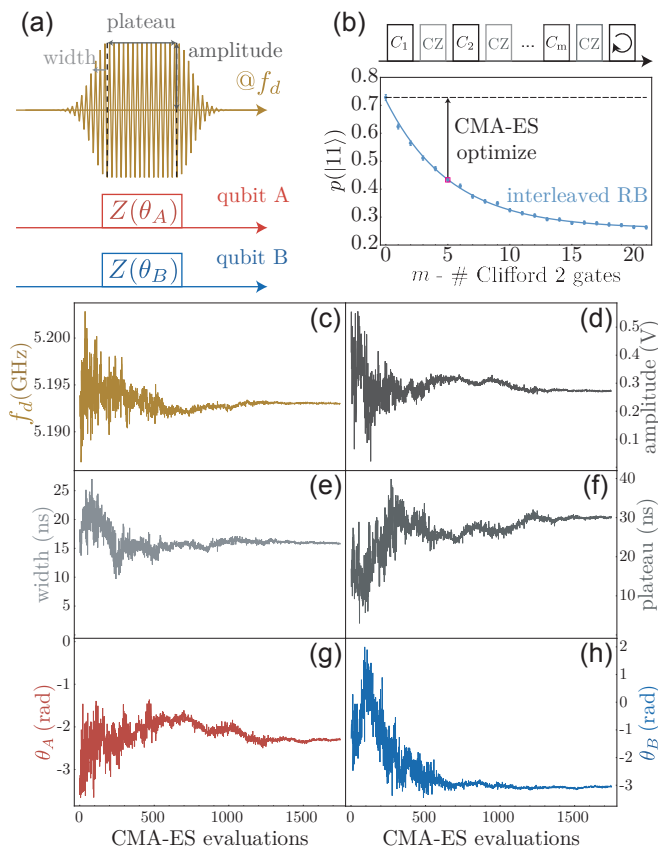


FIG. 5. Optimizing the CZ gate. (a) The gate is optimized over 6 parameters : pulse width, plateau, amplitude, and frequency as well as single qubit Z rotation angles. (b) We use an approach based on Optimized Randomized Benchmarking for Immediate Tune-up (ORBIT) to optimize the sequence fidelity at fixed length with a CMA-ES optimization. The number of Clifford gates [here $5 \simeq -1/\log(p)$] is chosen to maximize the sensitivity of the tune-up procedure. (c)-(h) Stochastic evolution of the gate parameters versus the number of function evaluation. The fidelity of the CZ gate is improved from 0.967 to 0.992.

The state tomography is obtained by a maximum likelihood estimation similar to the one in Ref. [52] using an overcomplete set of 36 tomography pulses. We represent the quantum process [53] in the Pauli basis through the process tomography matrix χ [46] [Fig. 4(b)] and adjust the single qubit phases with virtual Z rotations to attribute the relative phase accumulation to the $|11\rangle$ state only. We obtain process fidelity $F_{\text{QPT}} = 0.97$. This result shows that our scheme can be used to implement a CZ gate but the value of the fidelity is probably dominated by state preparation and measurement (SPAM) errors (Appendix C 2 and D) and cannot be used to optimize the gate parameters further.

Randomized benchmarking (RB) provides a reliable and robust metric of gate fidelity. The sequence is composed of m randomly chosen Clifford operations followed by a recovery gate aimed at bringing back the quan-

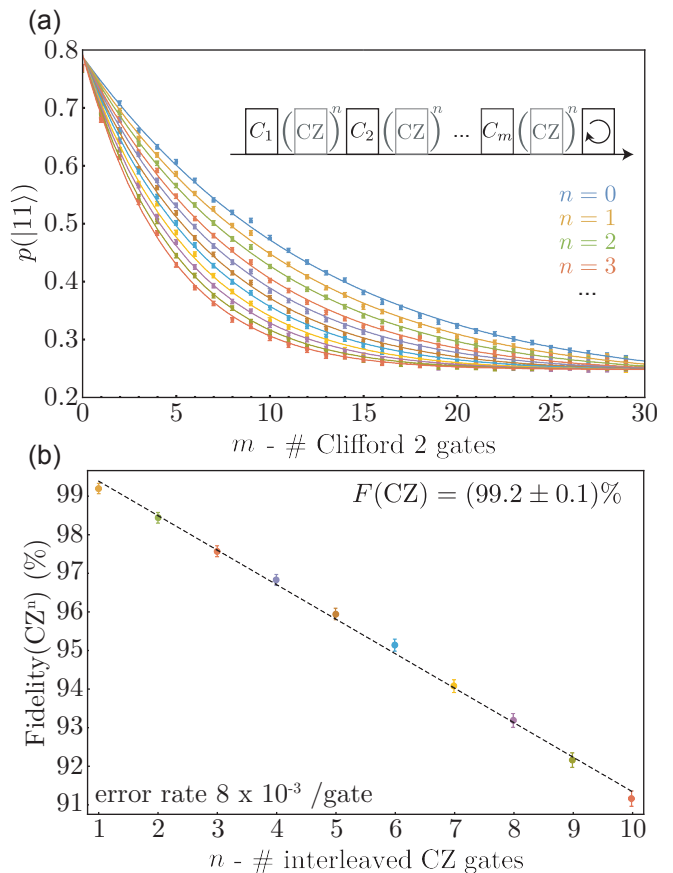


FIG. 6. Interleaved randomized benchmarking (a) Average probability $p(|11\rangle)$ as a function of sequence length. For each sequence length, we average over 100 random sequences repeated 1500 times. We insert a variable number $n = 0, 1, \dots, 10$ (encoded in the color) of CZ gates between the randomly chosen Clifford gates. (b) Fidelity of CZ^n versus n . The gate error grows linearly with n indicating that the errors are incoherent. Error bars are calculated according to the procedure given in Appendix E.

tum state to the initial state. The average population of $|11\rangle$ state decays as $a + bp^m + c(m-1)p^{m-2}$ where m is the number of Clifford operations, p is the depolarizing parameter and a, b, c are fitting parameters used to absorb state preparation and measurement errors [54]. The average fidelity of a Clifford operation is given by $F_{\text{Clifford}} = 1 - \frac{d-1}{d}(1-p)$ where $d = 2^n$ is the dimension of the Hilbert space with $n = 2$ the number of qubits. Interleaving a target gate yields a decay with depolarizing parameter p_{gate} and a gate error of $1 - F = \frac{d-1}{d}(1 - p_{\text{gate}}/p)$.

To reach the optimal gate fidelity, we perform a parameter search optimizing the sequence fidelity of fixed length interleaved randomized sequences [54] using a method known as 'Optimized Randomized Benchmarking for Immediate Tune-up' (ORBIT) [55] with a Covariance Matrix Adaptation Evolution Strategy (CMA-ES) [56]. In practice, we first measure an interleaved randomized benchmarking curve [see Fig. 5(b)] before fixing

the number of gates to $n = \text{floor}[-1/\log(p)] = 5$ providing the optimal sensitivity. The survival probability $p(|11\rangle)$ is maximized by adjusting the 6 gate parameters [Fig. 5(a)]: amplitude, duration, width of the edges, frequency, and single-qubit rotation angles. Fig. 5(c-h) shows the stochastic evolution of gate parameters during 1700 search steps leading to an improvement of gate fidelity from 0.967 to 0.992 for final gate duration of $30.0(\text{plateau}) + 2 \times 15.8(\text{edges}) = 61.6$ ns. In our experiment, CMA evolution strategy leads systematically to the same (global) minimum contrary to non-stochastic algorithm such as Nelder-Mead method that gets more easily trapped in local minima.

Finally, we assess the quality of the optimized CZ gate by iterative interleaved randomized benchmarking [54]. We obtain a reference fidelity $F_{\text{Clifford2}} = (96.0 \pm 0.1)\%$. Interleaving the CZ gate [yellow curve in Fig. 6(a)] yields a gate fidelity of $F(\text{CZ}) = (99.2 \pm 0.1)\%$. This measurement is repeated for an increasing number of interleaved CZ gates [Fig. 6(b)] to separate the contribution of systematic coherent errors from decoherence effects [57]. In our experiment, the total error of the CZ gate repeated n times grows linearly with the number of gates [Fig 6(b)] demonstrating that the remaining error is incoherent and thus not correctable with coherent controls.

V. OUTLOOK

Although the benchmarked fidelity of our CZ-gate is already high, the current experimental setup contains a number of imperfections, most of which can be readily eliminated in the next generation experiments. Let us start the discussion by briefly summarising these imperfections.

Taking into account the Ramsey coherence times of transitions $|10\rangle - |20\rangle$ and $|11\rangle - |21\rangle$ (see Table II), one expects the gate error bounded by 0.7% (see Appendix F 2). This estimate is compatible with the gate error $(0.8 \pm 0.1)\%$ measured with randomized benchmarking. We believe that the limited coherence time of our higher-level transitions originates in the first order sensitivity to external flux noise caused by the sweet spot misalignment. This effect can be corrected by either improving magnetic field uniformity, likely through better magnetic shielding, or by using two independent coils. Importantly, fluxonium's $|1\rangle - |2\rangle$ transition is very similar in term of decoherence mechanisms to a regular transmon transition [22] and we therefore expect no fundamental obstacles in reaching coherence times around $50 - 100 \mu\text{s}$, on par with optimally fabricated flux-tunable transmons. In this case, the Hamiltonian simulations presented in Fig. 3 shows that coherent gate errors in the low 10^{-4} -range are possible for our device without sophisticated pulse optimization.

Coherence time in the computational subspace can exceed $500 \mu\text{s}$, given the measured energy relaxation times of $250 - 350 \mu\text{s}$ of states $|10\rangle$ and $|01\rangle$. The proof-

of-principle demonstration of $T_2 \approx 500 \mu\text{s}$ coherence time was reported in a previous single-fluxonium experiment. Yet, here the qubit coherence time is reduced to $50 - 60 \mu\text{s}$, even at their flux sweet-spots. This is likely due to a residual average thermal photon population $n_{\text{th}} \sim 5 \times 10^{-3}$ in the readout resonator. Coherence time of the gating transitions $|10\rangle - |20\rangle$ and $|11\rangle - |21\rangle$ will be limited eventually by thermal dephasing as well. This dephasing source is generic to all superconducting circuit experiments and it can be mitigated in the future with improved cryogenic filtering of the microwave measurement lines [58, 59]. After this technical task is accomplished, the qubits in our gate scheme would be considerably better than transmons at storing quantum information in between the two-qubit gate operations.

Turning to our microwave packaging choice, we used a single input port in a single 3D-box resonator to perform all the gates, for the sake of technical simplicity (see Appendix B). In Appendix D, we characterize the reduction of addressability in the system and find that simultaneous single qubit gates have about a $\sim 3\%$ error rate dominated by classical cross-talks. Using a dedicated driving port per qubit would enable selective addressing of each qubit and hence improve significantly the single qubit gates fidelity [60]. More generally, individual addressing and readout is essential for scaling beyond the two-qubit experiments. We believe that scaling of our gate scheme can be done by simply moving to 2D-circuit designs, in complete analogy with processors based on capacitively-coupled transmon circuits [2–4]. Indeed, our experiment does not benefit from the usually high quality factors of 3D-resonators, and hence it is compatible with a traditional 2D-circuit technology without conceptual modifications. The only explicit price of replacing fixed-frequency transmons by fluxoniums would be the requirement of either a highly homogeneous global magnetic field or a static flux-bias line per qubit.

As a final remark, we stress that our CZ-gate does not require excessive parameter matching, unlike the majority of microwave-activated gates [34, 61]. For example, the level diagram in Fig. 1 has no fine-tuned transitions, and the described gate protocol would work for a large class of fluxonium spectra and interaction strengths. Essentially, one only need to make sure the states $|12\rangle$ and $|21\rangle$ are not too far from each other (around 300 MHz here) and that qubit frequencies are well resolved (about 70 MHz here). This property can mitigate the effects of fabrication imperfections and improve qubit connectivity in the large-scale quantum processors.

VI. CONCLUSIONS

In this paper, we demonstrated that low-frequency fluxonium qubits are not only good at storing quantum information, but they also allow for fast and high-fidelity logical operations with a minimal engineering overhead. Our implementation of the microwave-activated CZ gate

can be decomposed into two ideas applicable to other quantum systems, each harnessing the strong anharmonicity of fluxoniums. First, the energy scale Δ limiting the gate speed comes from the repulsion of non-computational states (here the repulsion of states $|21\rangle$ and $|12\rangle$), and hence the gate time $\sim 1/\Delta$ can be made, in principle, shorter than the qubit's Larmor periods. Second, by synchronizing Rabi rotations of the only two relevant non-computational transitions (here $|10\rangle - |20\rangle$ and $|11\rangle - |21\rangle$), a conditional geometric phase is accumulated at the end of each Rabi period with zero leakage outside the computational manifold. Notably, the synchronization is possible with a single microwave pulse of proper amplitude, frequency, and duration, applied to either qubit. We adjusted the conditional phase to π to get the CZ-gate, but the phase can be changed to any other value, resulting in the CPhase-gate.

We exhaustively characterized the CZ gate using both quantum process tomography and randomized benchmarking techniques. While the current combination of gate time, 61.6 ns, and gate infidelity, 8×10^{-3} , is already competitive with gates on transmons, our analysis indicates that the error can be reduced by an order of magnitude on improving the fabrication procedures, magnetic shielding, and line filtering. Given the compatibility of our capacitive coupling scheme with transmon-based scaling technology, we believe that all necessary demonstrations have been made to start exploring large-scale fluxonium-based quantum processors.

ACKNOWLEDGMENTS

We thank Chen Wang, Benjamin Huard, and Ivan Pechenezhskiy for useful discussions and acknowledge the support from NSF PFC at JQI and ARO-LPS HiPS program. V.E.M. and M.G.V acknowledge the Faculty Research Award from Google and fruitful conversations with the members of the Google Quantum AI team.

Appendix A: Device design and fabrication

The device is fabricated by standard e-beam lithography of a resist bilayer (MAA/PMMA) deposited on a high-resistivity silicon substrate. Two layers of Aluminum (20 and 40 nm) [22] separated by a thin barrier of oxide are deposited by double angle evaporation. Each inductance is composed of 310 (qubit A) and 206 (qubit B) identical Josephson junction (in agreement with the extracted parameters $E_{L,B}/E_{L,A} \simeq 206/310$). The loops are closed by a small Josephson junctions whose insulating barrier parameters determines $E_{J,A(B)}$. The antennas are designed to provide a charging energy $E_{C,A}, E_{C,B} \simeq 1$ GHz required to bring the second excited state transitions in the range 4 – 5 GHz. The asymmetry in the antenna design enables us to independently adjust the charging energy and the coupling to the cavity mode.

Table II gives the value of the energy relaxation and coherence times of the selected transitions of the system. All the lifetimes and coherence times are measured by energy relaxation, Ramsey and spin echo sequences. The reduced coherence time of the $|10\rangle - |20\rangle$ and $|11\rangle - |21\rangle$ is limiting the gate fidelity (see main text).

Transition	freq (GHz)	T_1 (μ s)	T_2^R (μ s)	T_2^E (μ s)
$ 00\rangle - 10\rangle$	0.07233	347	5.6	31
$ 00\rangle - 01\rangle$	0.13641	282	25.4	64
$ 10\rangle - 20\rangle$	5.1766	8.9	2.5	9.3
$ 11\rangle - 21\rangle$	5.1986	6.1	1.7	4.3

TABLE II. Frequencies and coherence times of transitions participating in the gate operation.

Appendix B: Measurement setup and wiring

Qubit pulses are directly generated by an Arbitrary Waveform Generator (see Fig. 7) instead of modulating a radio frequency tone. Our ability to multiplex and synthesize qubit pulses with a single digital-to-analog converter significantly reduces the hardware cost of the experiment. We use the internal mixing and pulse modulation capabilities of two Rhode and Schwarz®SMB100A sources to generate the readout pulse and the two qubit operations. The output signal is amplified by a Josephson Traveling Wave Parametric Amplifier (JTWPA) provided by Lincoln Labs [50] followed by commercial amplifiers before heterodyne detection.

Appendix C: Initialization and readout

1. Single-shot readout

Both fluxoniums are strongly coupled to a 3D cavity. We perform a joint readout [27, 62] of the qubit states. In the dispersive regime [63], the readout operator can be written

$$\hat{M} = \beta_{IZ}\mathbb{I} \otimes \sigma_Z + \beta_{ZI}\sigma_Z \otimes \mathbb{I} + \beta_{ZZ}\sigma_Z \otimes \sigma_Z \quad (\text{C1})$$

where β_{ij} are complex coefficients and σ_i are Pauli matrices. In the single-shot limit, the integrated heterodyne signal distribution can be modeled as the sum of four Gaussian distributions associated to the computational states $|00\rangle$, $|10\rangle$, $|01\rangle$, $|11\rangle$ (see Fig. 8).

Surprisingly, we observe that the populations (Fig. 8) extracted from fitting the readout distribution by four Gaussians are affected by the readout amplitude and duration indicating that our readout scheme is not Quantum Non-Demolition (QND) [64–66]. Fig. 9 represents the evolution of the population with the duration of a cavity pulse preceding the readout pulse.

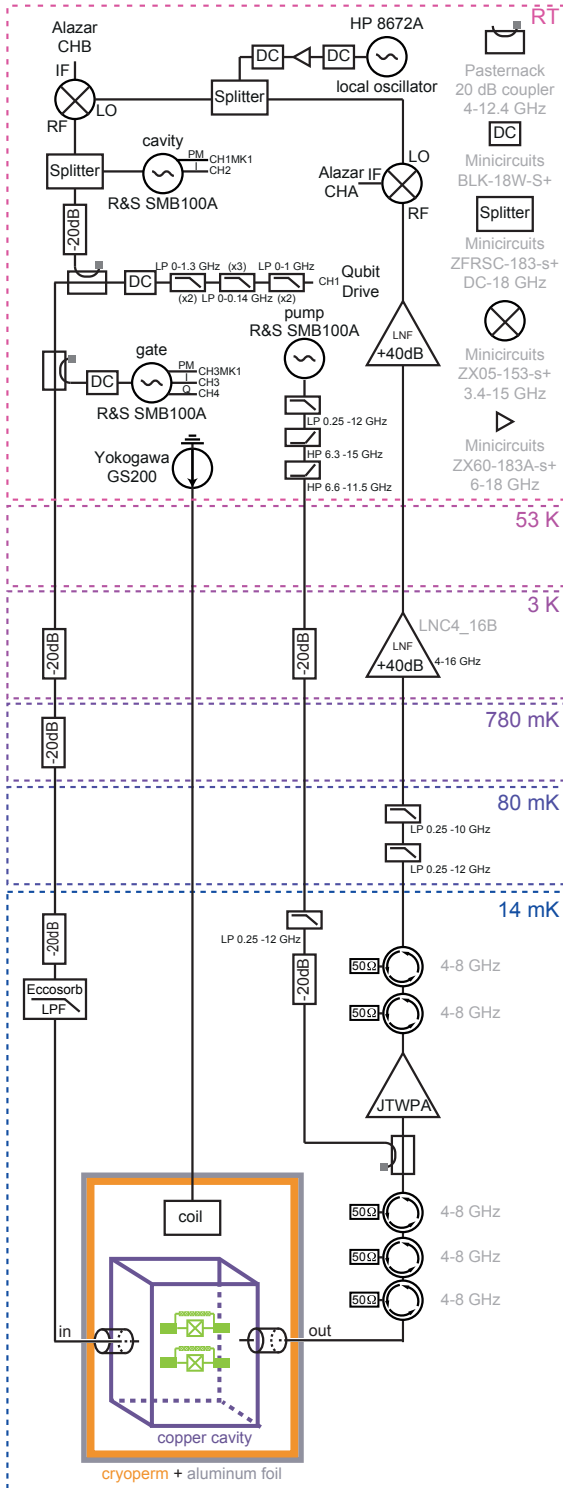


FIG. 7. Schematics of the experimental setup. Single qubit pulses are generated directly at the qubit frequencies using one analog output port of a Tektronix® Arbitrary Waveform Generator AWG5014C (not represented). The signal is combined with CZ gate pulses and readout pulses before reaching the input port of the 3D cavity. The outgoing signal is amplified using a Traveling Wave Parametric Amplifier followed by cryogenic and room temperature amplifiers before down-conversion by a local oscillator, digitization by an Alazar® acquisition board (not represented), and numerical demodulation.

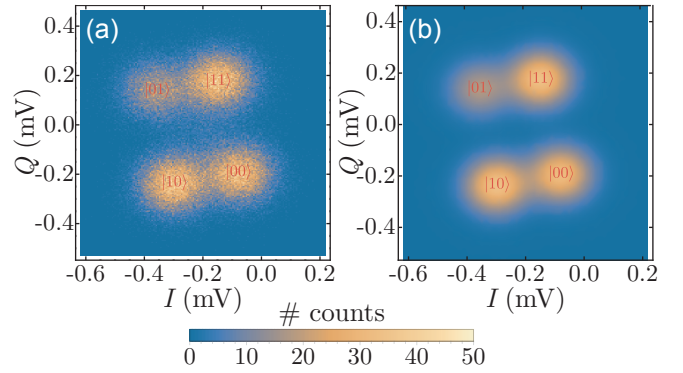


FIG. 8. Experimental (a) and fitted (b) single-shot histograms of the readout signal when the two qubits are in thermal equilibrium. Histograms in (a) are calculated from 1.5×10^5 experimental realizations with a $10 \mu\text{s}$ -long readout pulse. The fitting function is the sum of four gaussian distributions. This measurement is used to calibrate the position of the center of the gaussian distributions.

Although recent studies demonstrated the QND readout of granular aluminum fluxonium circuits with hundreds of photons [67], the non-QNDness of the readout of junction based fluxoniums was observed in the past either directly [68] or in the form of a qubit lifetime suppression by readout photons [69] even for average stationary photon number of the order of unity. These mechanisms are not investigated here and will be the subject of further studies.

2. Readout cross-talks compensation

We adopt an empirical readout cross-talk compensation introduced in Ref. [37]. This approach was used to compensate incorrect state mapping during a bifurcation readout but we believe that it is relevant in our case. First, we compensate for an incorrect mapping $|0\rangle \rightarrow |1\rangle$ or $|1\rangle \rightarrow |0\rangle$ of qubit α by correcting qubit population of states $|ij\rangle$ with a tensorial products of two 2×2 matrices $C_A \otimes C_B$ where $C_\alpha = \begin{pmatrix} a_\alpha & 1 - b_\alpha \\ 1 - a_\alpha & b_\alpha \end{pmatrix}$ where $a_{A(B)} = 0.98(0.96)$ and $b_{A(B)} = 0.96(0.87)$.

In addition, we use a pure cross-talk matrix which takes into account the possibility to swap excitations between the qubits during the readout process. The total readout correction applied to the qubit populations reads

$$\begin{pmatrix} p'_{00} \\ p'_{10} \\ p'_{01} \\ p'_{11} \end{pmatrix} = \begin{pmatrix} 1 & 0 & 0 & 0 \\ 0 & 1 - b & c & 0 \\ 0 & b & 1 - c & 0 \\ 0 & 0 & 0 & 1 \end{pmatrix} (C_A \otimes C_B) \begin{pmatrix} p_{00} \\ p_{10} \\ p_{01} \\ p_{11} \end{pmatrix} \quad (\text{C2})$$

where p'_{ij} are the corrected qubit populations, $b = 7\%$ and $c = 3.5\%$. The impact of this calibration is best exemplified when performing Rabi experiments. After the calibration (Fig. 10 right column), we observe that the

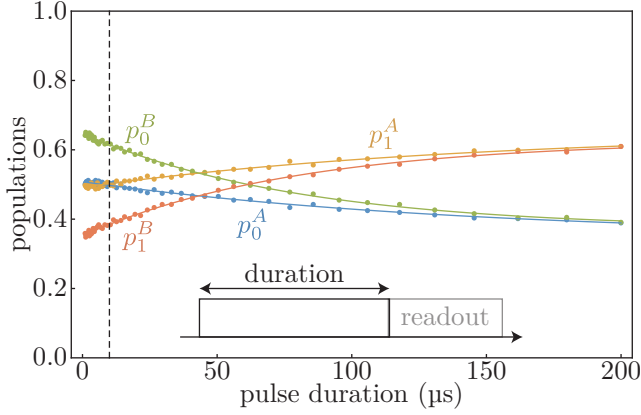


FIG. 9. Evolution of the qubit populations after a cavity pulse as a function of the pulse duration. The solid lines correspond to the solution of a rate equation Eq. C3 for each qubit with the transition rate $\Gamma_{\uparrow}^A = 4.4 \pm 0.1$ kHz, $\Gamma_{\downarrow}^A = 2.4 \pm 0.1$ kHz and $\Gamma_{\uparrow}^B = 7.83 \pm 0.05$ kHz, $\Gamma_{\downarrow}^B = 4.64 \pm 0.05$ kHz. The dashed line indicates the duration of the readout pulse. Note that the impact of the readout pulse in this figure is already corrected by the method described in section C 2.

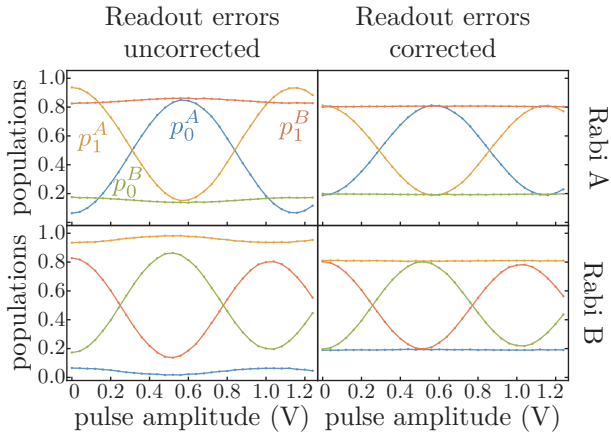


FIG. 10. Rabi oscillations of qubit A (first row) or qubit B (second row) without (left column) and with (right column) readout error correction. After the calibration, only the target qubit displays oscillations.

oscillations are centered around 0.5 (center of the Bloch sphere) and only the targeted qubit displays oscillations. Finally, we remind the reader that the two-qubit gate fidelities quoted in the main text are not affected by this procedure since randomized benchmarking is not sensitive to readout errors [70].

3. Initialization

We describe how we turned the qubit transitions induced by cavity photons observed in Fig. 9 to our advantage to initialize the system. The rate of these transitions is known to generally increase with the number of circu-

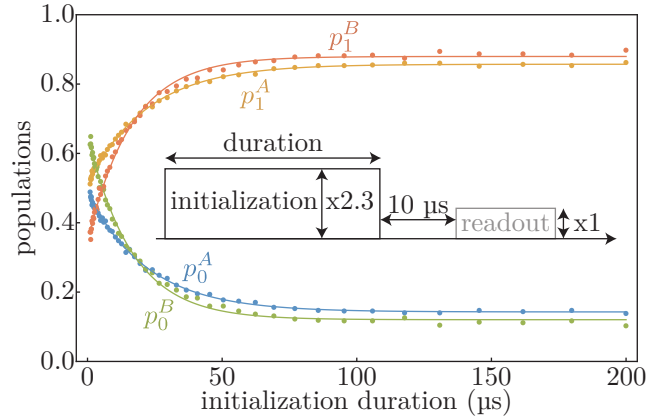


FIG. 11. Initialization of the two fluxoniums. We apply a large (2.3 times the readout amplitude) drive on the cavity in order to reduce the entropy of the system. Populations are extracted by the method described in section C 3. The solid lines correspond to a fit to rate equations for each qubit with following transition rates $\Gamma_{\uparrow}^A = 38.6 \pm 0.6$ kHz, $\Gamma_{\downarrow}^A = 6.4 \pm 0.6$ kHz and $\Gamma_{\uparrow}^B = 53.8 \pm 0.3$ kHz, $\Gamma_{\downarrow}^B = 7.4 \pm 0.3$ kHz. In all the measurements shown in this paper, we apply a 200 μ s initialization pulse that leaves the qubits in mixed states with excitation probability $p_1^A = 0.86$ and $p_1^B = 0.88$ that correspond to reversed thermal states with temperatures $T_A = 3.7$ mK and $T_B = 5.9$ mK. The entropy extracted by the initialization pulse is $\Delta S / \ln(2) = 0.81$ bits.

lating photons in the cavity [67, 69]. We thus expect to be able to induce incoherent transition rates between the qubit states.

We model the photon-induced relaxation using the incoherent rate equations

$$\begin{aligned} \frac{dp_0^\alpha}{dt} &= -\Gamma_{\uparrow}^\alpha p_0^\alpha + \Gamma_{\downarrow}^\alpha p_1^\alpha \\ \frac{dp_1^\alpha}{dt} &= \Gamma_{\uparrow}^\alpha p_0^\alpha - \Gamma_{\downarrow}^\alpha p_1^\alpha \end{aligned} \quad (\text{C3})$$

where the total excitation and de-excitation rates are $\Gamma_{\uparrow}^A = 38.6 \pm 0.6$ kHz, $\Gamma_{\downarrow}^A = 6.4 \pm 0.6$ kHz and $\Gamma_{\uparrow}^B = 53.8 \pm 0.3$ kHz, $\Gamma_{\downarrow}^B = 7.4 \pm 0.3$ kHz. Notably, increasing the number of circulating photons by a factor $2.3^2 \sim 5$ (from Fig. 9 to Fig. 11) increases the energy relaxation rates $\Gamma_{\downarrow}^A + \Gamma_{\uparrow}^A$ and $\Gamma_{\downarrow}^B + \Gamma_{\uparrow}^B$ by about a factor ~ 5 mainly by increasing the excitation rates. The amplitude of the initialization pulse was chosen to maximize the steady state purity while keeping the qubit populations in the computational space. This procedure leads to the preparation of the qubit states in a statistical mixture with the excited state probabilities $p_1^A = 0.86$ and $p_1^B = 0.88$ (see Fig. 11).

Appendix D: Single qubit gate fidelities

Single qubit gate fidelities are calibrated by single qubit randomized benchmarking (see Fig. 12). Qubit A

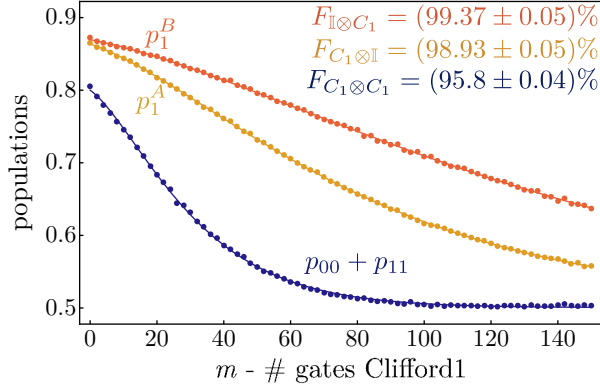


FIG. 12. Randomized benchmarking for single qubit gates on qubit A, qubit B and both. The solid lines are fit by a first order model [70] $a + bp^m + c(m-1)p^{m-2}$ where p is the depolarizing parameter used to calculate the fidelity $F = 1 - \frac{d-1}{d}(1-p)$ where d is the dimension of the Hilbert space. Error bars on the fidelity are calculated according to the procedure described in Appendix E.

(B) gates are generated using Gaussian edge pulses with a total duration of 150 ns (75 ns). Reducing the gate duration of single qubit gates deteriorates the simultaneous randomized benchmarking fidelity because of cross-talks.

The addressability of each qubit can be characterized by the numbers in table III using the definitions in Ref. [60]. The reduction of addressability in our system is related to the fact that our control field aimed at one target qubit is also influencing the other qubit (classical cross-talk) due to our choice of a sample design with a single input port.

parameter	Twirl group	experimental value
r_A	Clifford1 \otimes I	6.3×10^{-3}
r_B	I \otimes Clifford1	1.07×10^{-2}
$r_{A B}$	Clifford1 \otimes Clifford1	5.3×10^{-3}
$r_{B A}$	Clifford1 \otimes Clifford1	1.4×10^{-2}
$\delta r_{A B}$		8.1×10^{-3}
$\delta r_{B A}$		5.4×10^{-3}
δp		2.2×10^{-2}

TABLE III. Table of addressability metrics using the definition of Ref. [60]. The error rates r_α are extracted from the independent randomized benchmarking experiments of Fig. 12. The error rate $r_{\alpha|\beta}$ are extracted by looking at the depolarization of qubit α during a simultaneous randomized benchmarking experiment. The error metric of error on α due to the unwanted control of β is given by $\delta r_{\alpha|\beta} = |r_\alpha - r_{\alpha|\beta}|$. The correlations in errors are flagged by $\delta p = p_{AB} - p_{A|B}p_{B|A}$ where p_{AB} is obtained from fitting the decay of qubit-qubit correlations $p_{00} + p_{11}$.

The use of a first order model [70] to fit the randomized benchmarking decay can be justified by the presence of

a time-dependent gate dependent noise (flux noise) [71]. Table IV summarizes the fidelity of various gates used to generate the Clifford group.

gate	fidelity (%)
$X_{\pi/2} - \mathbb{I}$	97.9 ± 0.1
$Y_{\pi/2} - \mathbb{I}$	97.9 ± 0.1
$X_\pi - \mathbb{I}$	97.6 ± 0.1
$Y_\pi - \mathbb{I}$	97.6 ± 0.09
$\mathbb{I} - X_{\pi/2}$	98.95 ± 0.08
$\mathbb{I} - Y_{\pi/2}$	98.96 ± 0.08
$\mathbb{I} - X_\pi$	99.20 ± 0.08
$\mathbb{I} - Y_\pi$	99.20 ± 0.08
$X_{\pi/2} - X_{\pi/2}$	97.8 ± 0.1
$X_{\pi/2} - Y_{\pi/2}$	97.8 ± 0.1
$Y_{\pi/2} - X_{\pi/2}$	97.8 ± 0.1
$Y_{\pi/2} - Y_{\pi/2}$	97.8 ± 0.1
$X_\pi - X_\pi$	93.9 ± 0.2
$X_\pi - Y_\pi$	94.0 ± 0.2
$Y_\pi - X_\pi$	93.8 ± 0.2
$Y_\pi - Y_\pi$	94.2 ± 0.2

TABLE IV. Fidelities of various Clifford gates obtained by two-qubit interleaved randomized benchmarking.

Appendix E: Error bars

The error bars displayed in Fig. 6 are the standard deviations on the population obtained from the population extracted from the method described in Appendix C. All the curves in Fig. 6(a) are fitted simultaneously to a first order model $a + bp(n)^m + c(m-1)p(n)^{m-2}$ where a, b, c are fitting parameters used to absorb state preparation and measurement (SPAM) errors, m is the number of Clifford gates and n is the number of interleaved CZ gates. The fidelity of a n iteration of a CZ gate is given by $F(\text{CZ}^n) = 1 - \frac{d-1}{d} \left(1 - \frac{p(n)}{p(n=0)}\right)$ with $d = 4$.

The error on the gate fidelity is then estimated by the propagation of error formula

$$\Delta F(\text{CZ}^n) = \frac{d-1}{d} \sqrt{\left(\frac{\Delta p(n)}{p(n=0)}\right)^2 + \left(\frac{p(n)\Delta p(n=0)}{p(n=0)^2}\right)^2} \quad (\text{E1})$$

to obtain the error bars in Fig. 6(b). Similar procedures are used to obtain all the error bars given in the paper.

Appendix F: Theory and simulations of gate errors

1. Unitary errors

To study the unitary dynamics during the gate operation, we solve the Schrödinger equation numerically for the time-dependent Hamiltonian given by Eqs. (1)

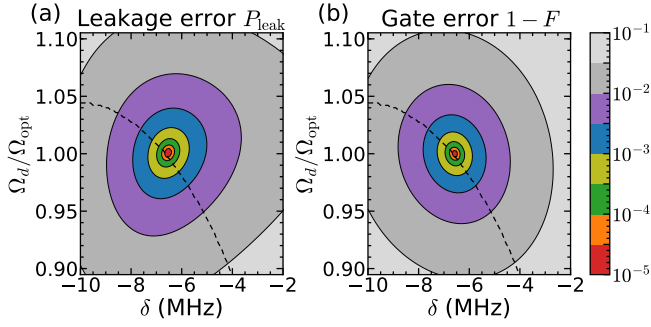


FIG. 13. Simulated leakage error (a) and gate error (b) for the total gate duration of $t_{\text{gate}} = 61$ ns vs drive-frequency detuning δ and drive amplitude Ω_d in units of its optimal value Ω_{opt} . Dashed lines show parameter values satisfying the correct phase accumulation $\Delta\varphi = \pi$.

and (2) with the additional account for a Gaussian flat-topped pulse in the drive term (2). Thus, we multiply the drive term by a pulse-shaping function with the rising edge given by

$$f(t) \propto \exp[-(t - t_{\text{width}})^2/2\sigma^2] - \exp[-t_{\text{width}}^2/2\sigma^2] \quad (\text{F1})$$

at $0 < t < t_{\text{width}}$, where $\sigma = t_{\text{width}}/\sqrt{2\pi}$. The lowering edge of the pulse is given by a symmetric expression at $t_{\text{width}} + t_{\text{plateau}} < t < t_{\text{gate}}$, where t_{plateau} is the duration of the flat part and $t_{\text{gate}} = 2t_{\text{width}} + t_{\text{plateau}}$ is the total gate duration. In all the simulations, we keep $t_{\text{width}} = 15$ ns and vary t_{plateau} in order to vary t_{gate} . To match the measured ratio between resonance Rabi frequencies Ω_{10-20} and Ω_{11-21} , we choose $\epsilon_A/\epsilon_B = 0.9$ in the drive term (2).

We find the evolution operator \hat{U} by calculating the evolution of four basis computational states, projecting the result into the computational subspace, and performing single-qubit Z rotations as described in Ref. [25], which ensures that the only diagonal matrix element that has a nonzero phase is $\langle 11|\hat{U}|11\rangle$. We then calculate the average gate fidelity as [72]

$$F = \frac{\text{Tr}(\hat{U}^\dagger \hat{U}) + |\text{Tr}(\hat{U}_{\text{CZ}}^\dagger \hat{U})|^2}{20}, \quad (\text{F2})$$

where $\hat{U}_{\text{CZ}} = \text{diag}(1, 1, 1, -1)$ is the diagonal operator for the ideal CZ gate. This expression corresponds to the randomized benchmarking fidelity [73]. When the real gate operator is $\hat{U} = \text{diag}(1, 1, 1, e^{i\Delta\varphi})$, we find that $1 - F = (3/10)(1 + \cos \Delta\varphi)$. For a generic gate operator, we define $\Delta\varphi = \arg\langle 11|\hat{U}|11\rangle$ and use the last expression to calculate the phase error, which is shown by dots in Fig. 3(c). Once projected into the computational subspace, the operator \hat{U} in Eq. (F2) is generally nonunitary, which describes coherent leakage to noncomputational levels. The average probability of such leakage is

given by

$$P_{\text{leak}} = 1 - \frac{1}{4} \text{Tr}(\hat{U}^\dagger \hat{U}). \quad (\text{F3})$$

We show this leakage error in Fig. 13(a) as well as by the dashed line in Fig. 3(c). The total gate error calculated using Eq. (F2) is shown in Fig. 13(b) and by the solid line in Fig. 3(c). Results shown in these figures illustrate that we can achieve coherent gate and leakage errors below 10^{-4} with the current amplitude and frequency stability of the experiment.

2. Decoherence effects

We estimate incoherent errors resulting from driving the $|10\rangle - |20\rangle$ and $|11\rangle - |21\rangle$ transitions as follows. We add the errors coming from cycling each transition independently. We first estimate the state fidelity for an arbitrary initial state when driving a full rotation on one of the transitions and average this fidelity over a set of 16 independent initial states before summing the two contributions. We solve the master equation by treating incoherent processes as a perturbation and write the density matrix as an expansion $\rho = \rho^{(0)} + \rho^{(1)} + \dots$. For the initial state $|\psi(0)\rangle = |\psi_\perp\rangle + c|11\rangle$, where $|\psi_\perp\rangle$ describes the amplitudes of the remaining computational basis states, we consider the Hilbert space with only three levels $|\psi_\perp\rangle$, $|11\rangle$, and $|21\rangle$. Here, $\langle \psi_\perp | \psi_\perp \rangle = 1 - |c|^2$. We consider the drive Hamiltonian on the $|11\rangle - |21\rangle$ transition in the interaction picture and under the rotating wave approximation

$$\begin{aligned} \frac{\hat{H}_\Omega}{\hbar} &= \frac{\Omega}{2} (|11\rangle\langle 21| + |21\rangle\langle 11|) \\ &= \frac{\Omega}{2} |+\rangle\langle +| - \frac{\Omega}{2} |-\rangle\langle -|, \end{aligned} \quad (\text{F4})$$

where we have introduced the basis $|\pm\rangle = (|11\rangle \pm |21\rangle)/\sqrt{2}$ that diagonalizes \hat{H}_Ω . The unitary evolution under this Hamiltonian results in

$$\begin{aligned} |\psi(t)\rangle &= |\psi_\perp\rangle + c [\cos(\pi\Omega t) |11\rangle - i \sin(\pi\Omega t) |21\rangle] \\ &= |\psi_\perp\rangle + c \left[\frac{e^{-i\pi\Omega t}}{\sqrt{2}} |+\rangle + \frac{e^{i\pi\Omega t}}{\sqrt{2}} |-\rangle \right], \end{aligned} \quad (\text{F5})$$

which gives us the zeroth-order approximation to the density matrix $\rho^{(0)}(t) = |\psi(t)\rangle\langle\psi(t)|$. We find the first-order correction $\rho^{(1)}(t)$ from the iterative master equation

$$\frac{d\rho^{(1)}}{dt} = -\frac{i}{\hbar} [\hat{H}_\Omega, \rho^{(1)}(t)] + \mathcal{L}\rho^{(0)}(t), \quad (\text{F6})$$

where the Lindblad super-operator $\mathcal{L}\rho = \sum_k [\hat{L}_k \rho \hat{L}_k^\dagger - (1/2)(\hat{L}_k^\dagger \hat{L}_k \rho + \rho \hat{L}_k^\dagger \hat{L}_k)]$ describes nonunitary processes. We use the following collapse operators

$$\hat{L}_1 = \sqrt{\Gamma_1}|11\rangle\langle 21|, \quad (\text{F7a})$$

$$\hat{L}_\varphi = \sqrt{2\Gamma_\varphi}|21\rangle\langle 21|. \quad (\text{F7b})$$

The first operator describes relaxation of the $|11\rangle - |21\rangle$ transition with a rate $\Gamma_1 = 1/T_1(11 - 21)$, and the second operator describes pure dephasing with a rate $\Gamma_\varphi = 1/T_2^R(11 - 21) - 1/2T_1(11 - 21)$ (see Table II).

This gives the matrix element of the correction in the basis diagonalizing \hat{H}_Ω

$$\langle m | \rho^{(1)}(t) | n \rangle = \int_0^t \langle m | \mathcal{L}\rho^{(0)}(t') | n \rangle e^{-i\nu_{mn}(t-t')} dt', \quad (\text{F8})$$

where $h\nu_{mn} = E_m - E_n$ is the difference between eigenvalues of \hat{H}_Ω corresponding to $|m\rangle$ and $|n\rangle$. These eigenvalues belong to the set $\{\pm h\Omega/2, 0\}$.

Using these operators and equations above, we find the following expression for the state-preparation error ($t_{\text{gate}} = 1/\Omega$):

$$1 - F_\psi = -\text{Tr} \left[\rho^{(0)}(t_{\text{gate}})\rho^{(1)}(t_{\text{gate}}) \right] \\ = \frac{(\Gamma_1 + 2\Gamma_\varphi)t_{\text{gate}}}{2} |c|^2(1 - |c|^2) + \frac{(3\Gamma_1 + 2\Gamma_\varphi)t_{\text{gate}}}{8} |c|^4. \quad (\text{F9})$$

To find the gate error, we average Eq. (F9) over 16 initial two-qubit states generated from single-qubit states

$|0\rangle$, $|1\rangle$, $(|0\rangle + |1\rangle)/\sqrt{2}$, and $(|0\rangle + i|1\rangle)/\sqrt{2}$. This gives the average values $\langle |c|^2 \rangle = 1/4$ and $\langle |c|^4 \rangle = 9/64$, which results in the gate error

$$1 - F = \frac{(55\Gamma_1 + 74\Gamma_\varphi)t_{\text{gate}}}{512} = \frac{9}{256} \frac{t_{\text{gate}}}{T_1} + \frac{37}{256} \frac{t_{\text{gate}}}{T_2}, \quad (\text{F10})$$

where we have used the relations $\Gamma_1 = 1/T_1$ and $\Gamma_\varphi = 1/T_2 - 1/2T_1$. The upper bound for the contribution coming from the $|10\rangle - |20\rangle$ has the same form.

Comparing the values of T_1 and Ramsey T_2 in Table II, we find that the main contribution is coming from T_2 , so $1 - F \approx (37/256)t_{\text{gate}}/T_2 \approx 0.15t_{\text{gate}}/T_2$. Then, for $t_{\text{gate}} = 1/\Delta = 45.5$ ns (our analysis is valid for a square pulse), we find that $1 - F \approx 0.15t_{\text{gate}}(1/T_2^R(10 - 20) + 1/T_2^R(11 - 21)) \approx 0.67\%$.

As a sanity check, we have also integrated numerically the master equation in the six-level Hilbert space that consists of the computational subspace and two upper levels $|20\rangle$ and $|21\rangle$. We considered the Hamiltonian generalized from Eq. (F4) to include the drive of the $|10\rangle - |20\rangle$ transition and to account for detunings between the drive frequency and two transition frequencies as described in Sec. III. Using collapse operators given in Eqs. (F7a) and (F7b) and similar operators for the $|10\rangle - |20\rangle$ transition, we find the incoherent error to be 0.64%, which is close to the analytic estimate of 0.67%.

-
- [1] Morten Kjaergaard, Mollie E. Schwartz, Jochen Braumüller, Philip Krantz, Joel I.J. Wang, Simon Gustavsson, and William D. Oliver, “Superconducting Qubits: Current State of Play,” Annual Review of Condensed Matter Physics **11**, 369–395 (2020).
- [2] J. Kelly, R. Barends, A. G. Fowler, A. Megrant, E. Jeffrey, T. C. White, D. Sank, J. Y. Mutus, B. Campbell, Yu Chen, Z. Chen, B. Chiaro, A. Dunsworth, I. C. Hoi, C. Neill, P. J.J. O’Malley, C. Quintana, P. Roushan, A. Vainsencher, J. Wenner, A. N. Cleland, and John M. Martinis, “State preservation by repetitive error detection in a superconducting quantum circuit,” Nature **519**, 66–69 (2015).
- [3] J. S. Otterbach, R. Manenti, N. Alidoust, A. Bestwick, M. Block, B. Bloom, S. Caldwell, N. Didier, E. Schuyler Fried, S. Hong, P. Karalekas, C. B. Osborn, A. Pappageorge, E. C. Peterson, G. Prawiroatmodjo, N. Rubin, Colm A. Ryan, D. Scarabelli, M. Scheer, E. A. Sete, P. Sivarajah, Robert S. Smith, A. Staley, N. Tezak, W. J. Zeng, A. Hudson, Blake R. Johnson, M. Reagor, M. P. da Silva, and C. Rigetti, “Unsupervised Machine Learning on a Hybrid Quantum Computer,” arXiv:1712.05771 (2017).
- [4] Abhinav Kandala, Antonio Mezzacapo, Kristan Temme, Maika Takita, Markus Brink, Jerry M. Chow, and Jay M. Gambetta, “Hardware-efficient variational quantum eigensolver for small molecules and quantum magnets,” Nature **549**, 242–246 (2017).
- [5] Chao Song, Kai Xu, Wuxin Liu, Chui Ping Yang, Shi Biao Zheng, Hui Deng, Qiwei Xie, Keqiang Huang, Qiujiang Guo, Libo Zhang, Pengfei Zhang, Da Xu, Dongning Zheng, Xiaobo Zhu, H. Wang, Y. A. Chen, C. Y. Lu, Siyuan Han, and Jian Wei Pan, “10-Qubit Entanglement and Parallel Logic Operations with a Superconducting Circuit,” Physical Review Letters **119**, 180511 (2017).
- [6] C. Neill, P. Roushan, K. Kechedzhi, S. Boixo, S. V. Isakov, V. Smelyanskiy, A. Megrant, B. Chiaro, A. Dunsworth, K. Arya, R. Barends, B. Burkett, Y. Chen, Z. Chen, A. Fowler, B. Foxen, M. Giustina, R. Graff, E. Jeffrey, T. Huang, J. Kelly, P. Klimov, E. Lucero, J. Mutus, M. Neeley, C. Quintana, D. Sank, A. Vainsencher, J. Wenner, T. C. White, H. Neven, and J. M. Martinis, “A blueprint for demonstrating quantum supremacy with superconducting qubits,” Science **360**, 195–199 (2018).
- [7] Ken X. Wei, Isaac Lauer, Srikanth Srinivasan, Neereja Sundaresan, Douglas T. McClure, David Toyli, David C. McKay, Jay M. Gambetta, and Sarah Sheldon, “Verifying multipartite entangled Greenberger-Horne-Zeilinger

- states via multiple quantum coherences,” *Physical Review A* **101**, 032343 (2020).
- [8] Petar Jurcevic, Ali Javadi-Abhari, Lev S. Bishop, Isaac Lauer, Daniela F. Bogorin, Markus Brink, Lauren Capelluto, Oktay Günlük, Toshinari Itoko, Naoki Kanazawa, Abhinav Kandala, George A. Keefe, Kevin Krsulich, William Landers, Eric P. Lewandowski, Douglas T. McClure, Giacomo Nannicini, Adinath Narasgond, Hasan M. Nayfeh, Emily Pritchett, Mary Beth Rothwell, Srikanth Srinivasan, Neereja Sundaresan, Cindy Wang, Ken X. Wei, Christopher J. Wood, Jeng-Bang Yau, Eric J. Zhang, Oliver E. Dial, Jerry M. Chow, and Jay M. Gambetta, “Demonstration of quantum volume 64 on a superconducting quantum computing system,” arXiv:2008.08571 (2020).
- [9] Akel Hashim, Ravi K. Naik, Alexis Morvan, Jean-Loup Ville, Bradley Mitchell, John Mark Kreikebaum, Marc Davis, Ethan Smith, Costin Iancu, Kevin P. O’Brien, Ian Hincks, Joel J. Wallman, Joseph Emerson, and Irfan Siddiqi, “Randomized compiling for scalable quantum computing on a noisy superconducting quantum processor,” arXiv:2010.00215 (2020).
- [10] Nissim Ofek, Andrei Petrenko, Reinier Heeres, Philip Reinhold, Zaki Leghtas, Brian Vlastakis, Yehan Liu, Luigi Frunzio, S. M. Girvin, L. Jiang, Mazyar Mirrahimi, M. H. Devoret, and R. J. Schoelkopf, “Extending the lifetime of a quantum bit with error correction in superconducting circuits,” *Nature* **536**, 441–445 (2016).
- [11] U. Las Heras, A. Mezzacapo, L. Lamata, S. Filipp, A. Wallraff, and E. Solano, “Digital quantum simulation of spin systems in superconducting circuits,” *Physical Review Letters* **112**, 200501 (2014).
- [12] Y. Salathé, M. Mondal, M. Opliger, J. Heinsoo, P. Kurpiers, A. Potočnik, A. Mezzacapo, U. Las Heras, L. Lamata, E. Solano, S. Filipp, and A. Wallraff, “Digital quantum simulation of spin models with circuit quantum electrodynamics,” *Physical Review X* **5**, 021027 (2015).
- [13] R. Barends, A. Shabani, L. Lamata, J. Kelly, A. Mezzacapo, U. Las Heras, R. Babbush, A. G. Fowler, B. Campbell, Yu Chen, Z. Chen, B. Chiaro, A. Dunsworth, E. Jeffrey, E. Lucero, A. Megrant, J. Y. Mutus, M. Neeley, C. Neill, P. J.J. O’Malley, C. Quintana, P. Roushan, D. Sank, A. Vainsencher, J. Wenner, T. C. White, E. Solano, H. Neven, and John M. Martinis, “Digitized adiabatic quantum computing with a superconducting circuit,” *Nature* **534**, 222–226 (2016).
- [14] Frank Arute, Kunal Arya, Ryan Babbush, Dave Bacon, Joseph C. Bardin, Rami Barends, Andreas Bengtsson, Sergio Boixo, Michael Broughton, Bob B. Buckley, David A. Buell, Brian Burkett, Nicholas Bushnell, Yu Chen, Zijun Chen, Yu-An Chen, Ben Chiaro, Roberto Collins, Stephen J. Cotton, William Courtney, Sean Demura, Alan Derk, Andrew Dunsworth, Daniel Eppens, Thomas Ekl, Catherine Erickson, Edward Farhi, Austin Fowler, Brooks Foxen, Craig Gidney, Marissa Giustina, Rob Graff, Jonathan A. Gross, Steve Habegger, Matthew P. Harrigan, Alan Ho, Sabrina Hong, Trent Huang, William Huggins, Lev B. Ioffe, Sergei V. Isakov, Evan Jeffrey, Zhang Jiang, Cody Jones, Dvir Kafri, Kostyantyn Kechedzhi, Julian Kelly, Seon Kim, Paul V. Klimov, Alexander N. Korotkov, Fedor Kostritsa, David Landhuis, Pavel Laptev, Mike Lindmark, Erik Lucero, Michael Marthaler, Orion Martin, John M. Martinis, Anika Maruszczyk, Sam McArdle, Jarrod R. McClean, Trevor McCourt, Matt McEwen, Anthony Megrant, Carlos Mejuto-Zaera, Xiao Mi, Masoud Mohseni, Wojciech Mroczkiewicz, Josh Mutus, Ofer Naaman, Matthew Neeley, Charles Neill, Hartmut Neven, Michael Newman, Murphy Yuezhen Niu, Thomas E. O’Brien, Eric Ostby, Bálint Pató, Andre Petukhov, Harald Putterman, Chris Quintana, Jan-Michael Reiner, Pedram Roushan, Nicholas C. Rubin, Daniel Sank, Kevin J. Satzinger, Vadim Smelyanskiy, Doug Strain, Kevin J. Sung, Peter Schmitteckert, Marco Szalay, Norm M. Tubman, Amit Vainsencher, Theodore White, Nicolas Vogt, Z. Jamie Yao, Ping Yeh, Adam Zalcman, and Sebastian Zanker, “Observation of separated dynamics of charge and spin in the Fermi-Hubbard model,” arXiv:2010.07965 (2020).
- [15] Dmitry A. Fedorov, Matthew J. Otten, Stephen K. Gray, and Yuri Alexeev, “Ab Initio Molecular Dynamics on Quantum Computers,” arXiv:2008.06562 (2020).
- [16] Benedikt Fauseweh and Jian-Xin Zhu, “Digital Quantum Simulation of Non-Equilibrium Quantum Many-Body Systems,” arXiv:2009.07375 (2020).
- [17] R. Barends, L. Lamata, J. Kelly, L. García-Álvarez, A. G. Fowler, A. Megrant, E. Jeffrey, T. C. White, D. Sank, J. Y. Mutus, B. Campbell, Yu Chen, Z. Chen, B. Chiaro, A. Dunsworth, I. C. Hoi, C. Neill, P. J.J. O’Malley, C. Quintana, P. Roushan, A. Vainsencher, J. Wenner, E. Solano, and John M. Martinis, “Digital quantum simulation of fermionic models with a superconducting circuit,” *Nature Communications* **6**, 7654 (2015).
- [18] Nikolaj Moll, Panagiotis Barkoutsos, Lev S. Bishop, Jerry M. Chow, Andrew Cross, Daniel J. Egger, Stefan Filipp, Andreas Fuhrer, Jay M. Gambetta, Marc Ganzhorn, Abhinav Kandala, Antonio Mezzacapo, Peter Müller, Walter Riess, Gian Salis, John Smolin, Ivano Tavernelli, and Kristan Temme, “Quantum optimization using variational algorithms on near-term quantum devices,” *Quantum Science and Technology* **3**, 030503 (2018).
- [19] Frank Arute, Kunal Arya, Ryan Babbush, Dave Bacon, Joseph C. Bardin, Rami Barends, Sergio Boixo, Michael Broughton, Bob B. Buckley, David A. Buell, Brian Burkett, Nicholas Bushnell, Yu Chen, Zijun Chen, Ben Chiaro, Roberto Collins, William Courtney, Sean Demura, Andrew Dunsworth, Daniel Eppens, Edward Farhi, Austin Fowler, Brooks Foxen, Craig Gidney, Marissa Giustina, Rob Graff, Steve Habegger, Matthew P. Harrigan, Alan Ho, Sabrina Hong, Trent Huang, L. B. Ioffe, Sergei V. Isakov, Evan Jeffrey, Zhang Jiang, Cody Jones, Dvir Kafri, Kostyantyn Kechedzhi, Julian Kelly, Seon Kim, Paul V. Klimov, Alexander N. Korotkov, Fedor Kostritsa, David Landhuis, Pavel Laptev, Mike Lindmark, Martin Leib, Erik Lucero, Orion Martin, John M. Martinis, Jarrod R. McClean, Matt McEwen, Anthony Megrant, Xiao Mi, Masoud Mohseni, Wojciech Mroczkiewicz, Josh Mutus, Ofer Naaman, Matthew Neeley, Charles Neill, Florian Neukart, Hartmut Neven, Murphy Yuezhen Niu, Thomas E. O’Brien, Bryan O’Gorman, Eric Ostby, Andre Petukhov, Harald Putterman, Chris Quintana, Pedram Roushan, Nicholas C. Rubin, Daniel Sank, Kevin J. Satzinger, Andrea Skolik, Vadim Smelyanskiy, Doug Strain, Michael Streif, Kevin J. Sung, Marco Szalay, Amit Vainsencher, Theodore White, Z. Jamie Yao, Ping Yeh, Adam Zalcman, and Leo Zhou, “Quantum Approx-

- imate Optimization of Non-Planar Graph Problems on a Planar Superconducting Processor,” arXiv:2004.04197 (2020).
- [20] Frank Arute, Kunal Arya, Ryan Babbush, Dave Bacon, Joseph C. Bardin, Rami Barends, Rupak Biswas, Sergio Boixo, Fernando G.S.L. Brandao, David A. Buell, Brian Burkett, Yu Chen, Zijun Chen, Ben Chiaro, Roberto Collins, William Courtney, Andrew Dunsworth, Edward Farhi, Brooks Foxen, Austin Fowler, Craig Gidney, Marissa Giustina, Rob Graff, Keith Guerin, Steve Habegger, Matthew P. Harrigan, Michael J. Hartmann, Alan Ho, Markus Hoffmann, Trent Huang, Travis S. Humble, Sergei V. Isakov, Evan Jeffrey, Zhang Jiang, Dvir Kafri, Kostyantyn Kechedzhi, Julian Kelly, Paul V. Klimov, Sergey Knysh, Alexander Korotkov, Fedor Kostritsa, David Landhuis, Mike Lindmark, Erik Lucero, Dmitry Lyakh, Salvatore Mandrà, Jarrod R. McClean, Matthew McEwen, Anthony Megrant, Xiao Mi, Kristel Michielsen, Masoud Mohseni, Josh Mutus, Ofer Naaman, Matthew Neeley, Charles Neill, Murphy Yuezhen Niu, Eric Ostby, Andre Petukhov, John C. Platt, Chris Quintana, Eleanor G. Rieffel, Pedram Roushan, Nicholas C. Rubin, Daniel Sank, Kevin J. Satzinger, Vadim Smelyanskiy, Kevin J. Sung, Matthew D. Trevithick, Amit Vainsencher, Benjamin Villalonga, Theodore White, Z. Jamie Yao, Ping Yeh, Adam Zalcman, Hartmut Neven, and John M. Martinis, “Quantum supremacy using a programmable superconducting processor,” *Nature* **574**, 505–510 (2019).
- [21] Jens Koch, Terri M. Yu, Jay Gambetta, A. A. Houck, D. I. Schuster, J. Majer, Alexandre Blais, M. H. Devoret, S. M. Girvin, and R. J. Schoelkopf, “Charge-insensitive qubit design derived from the Cooper pair box,” *Physical Review A - Atomic, Molecular, and Optical Physics* **76**, 042319 (2007).
- [22] Long B. Nguyen, Yen Hsiang Lin, Aaron Somoroff, Raymond Mencia, Nicholas Grabon, and Vladimir E. Manucharyan, “High-Coherence Fluxonium Qubit,” *Physical Review X* **9**, 041041 (2019).
- [23] Helin Zhang, Srivatsan Chakram, Tanay Roy, Nathan Earnest, Yao Lu, Ziwen Huang, Daniel Weiss, Jens Koch, and David I. Schuster, “Universal fast flux control of a coherent, low-frequency qubit,” arXiv:2002.10653 (2020).
- [24] Vladimir E. Manucharyan, Jens Koch, Leonid I. Glazman, and Michel H. Devoret, “Fluxonium: Single cooper-pair circuit free of charge offsets,” *Science* **326**, 113–116 (2009).
- [25] Konstantin N. Nesterov, Ivan V. Pechenezhskiy, Chen Wang, Vladimir E. Manucharyan, and Maxim G. Vavilov, “Microwave-activated controlled- Z gate for fixed-frequency fluxonium qubits,” *Physical Review A* **98**, 030301 (2018).
- [26] Frederick W. Strauch, Philip R. Johnson, Alex J. Dragt, C. J. Lobb, J. R. Anderson, and F. C. Wellstood, “Quantum logic gates for coupled superconducting phase qubits,” *Physical Review Letters* **91**, 167005 (2003).
- [27] L. Dicarlo, J. M. Chow, J. M. Gambetta, Lev S. Bishop, B. R. Johnson, D. I. Schuster, J. Majer, A. Blais, L. Frunzio, S. M. Girvin, and R. J. Schoelkopf, “Demonstration of two-qubit algorithms with a superconducting quantum processor,” *Nature* **460**, 240–244 (2009).
- [28] A. A. Abdumalikov, J. M. Fink, K. Juliusson, M. Pechal, S. Berger, A. Wallraff, and S. Filipp, “Experimental realization of non-Abelian non-adiabatic geometric gates,” *Nature* **496**, 482–485 (2013).
- [29] D. J. Egger and F. K. Wilhelm, “Optimized controlled-Z gates for two superconducting qubits coupled through a resonator,” *Superconductor Science and Technology* **27**, 014001 (2014).
- [30] R. Barends, C. M. Quintana, A. G. Petukhov, Yu Chen, D. Kafri, K. Kechedzhi, R. Collins, O. Naaman, S. Boixo, F. Arute, K. Arya, D. Buell, B. Burkett, Z. Chen, B. Chiaro, A. Dunsworth, B. Foxen, A. Fowler, C. Gidney, M. Giustina, R. Graff, T. Huang, E. Jeffrey, J. Kelly, P. V. Klimov, F. Kostritsa, D. Landhuis, E. Lucero, M. McEwen, A. Megrant, X. Mi, J. Mutus, M. Neeley, C. Neill, E. Ostby, P. Roushan, D. Sank, K. J. Satzinger, A. Vainsencher, T. White, J. Yao, P. Yeh, A. Zalcman, H. Neven, V. N. Smelyanskiy, and John M. Martinis, “Diabatic Gates for Frequency-Tunable Superconducting Qubits,” *Physical Review Letters* **123**, 210501 (2019).
- [31] S. Krinner, P. Kurpiers, B. Royer, P. Magnard, I. Tsitsilini, J. C. Besse, A. Remm, A. Blais, and A. Wallraff, “Demonstration of an All-Microwave Controlled-Phase Gate between Far Detuned Qubits,” arXiv:2006.10639 (2020).
- [32] M. Ganzhorn, G. Salis, D. J. Egger, A. Fuhrer, M. Mergenthaler, C. Müller, P. Müller, S. Paredes, M. Pechal, M. Werninghaus, and S. Filipp, “Benchmarking the noise sensitivity of different parametric two-qubit gates in a single superconducting quantum computing platform,” *Physical Review Research* **2**, 033447 (2020).
- [33] V. Negirneac, H. Ali, N. Muthusubramanian, F. Battistel, R. Sagastizabal, M. S. Moreira, J. F. Marques, W. Vlothuizen, M. Beekman, N. Haider, A. Bruno, and L. DiCarlo, “High-fidelity controlled-Z gate with maximal intermediate leakage operating at the speed limit in a superconducting quantum processor,” arXiv:2008.07411 (2020).
- [34] Jerry M. Chow, Jay M. Gambetta, Andrew W. Cross, Seth T. Merkel, Chad Rigetti, and M. Steffen, “Microwave-activated conditional-phase gate for superconducting qubits,” *New Journal of Physics* **15**, 115012 (2013).
- [35] Alexandre Blais, Alexander Maassen van den Brink, and Alexandre M. Zagoskin, “Tunable Coupling of Superconducting Qubits,” *Physical Review Letters* **90**, 4 (2003).
- [36] R. C. Bialczak, M. Ansmann, M. Hofheinz, E. Lucero, M. Neeley, A. D. Oconnell, D. Sank, H. Wang, J. Wenner, M. Steffen, A. N. Cleland, and J. M. Martinis, “Quantum process tomography of a universal entangling gate implemented with Josephson phase qubits,” *Nature Physics* **6**, 409–413 (2010).
- [37] A. Dewes, F. R. Ong, V. Schmitt, R. Lauro, N. Boulant, P. Bertet, D. Vion, and D. Esteve, “Characterization of a two-transmon processor with individual single-shot qubit readout,” *Physical Review Letters* **108**, 57002 (2012).
- [38] Chad Rigetti and Michel Devoret, “Fully microwave-tunable universal gates in superconducting qubits with linear couplings and fixed transition frequencies,” *Physical Review B - Condensed Matter and Materials Physics* **81**, 134507 (2010).
- [39] Jerry M. Chow, A. D. Córcoles, Jay M. Gambetta, Chad Rigetti, B. R. Johnson, John A. Smolin, J. R. Rozen, George A. Keefe, Mary B. Rothwell, Mark B. Ketchen, and M. Steffen, “Simple all-microwave entangling gate for fixed-frequency superconducting qubits,” *Physical Review Letters* **107**, 080502 (2011).

- [40] Sarah Sheldon, Easwar Magesan, Jerry M. Chow, and Jay M. Gambetta, “Procedure for systematically tuning up cross-talk in the cross-resonance gate,” *Physical Review A* **93**, 060302 (2016).
- [41] Neereja Sundaresan, Isaac Lauer, Emily Pritchett, Easwar Magesan, Petar Jurcevic, and Jay M. Gambetta, “Reducing unitary and spectator errors in cross resonance with optimized rotary echoes,” arXiv:2007.02925 (2020).
- [42] Pranav Mundada, Gengyan Zhang, Thomas Hazard, and Andrew Houck, “Suppression of Qubit Crosstalk in a Tunable Coupling Superconducting Circuit,” *Physical Review Applied* **12**, 054023 (2019).
- [43] X. Li, T. Cai, H. Yan, Z. Wang, X. Pan, Y. Ma, W. Cai, J. Han, Z. Hua, X. Han, Y. Wu, H. Zhang, H. Wang, Yipu Song, Luming Duan, and Luyan Sun, “Tunable Coupler for Realizing a Controlled-Phase Gate with Dynamically Decoupled Regime in a Superconducting Circuit,” *Physical Review Applied* **14**, 024070 (2020).
- [44] Atsushi Noguchi, Alto Osada, Shumpei Masuda, Shingo Kono, Kentaro Heya, Samuel Piotr Wolski, Hiroki Takahashi, Takanori Sugiyama, Dany Lachance-Quirion, and Yasunobu Nakamura, “Fast parametric two-qubit gates with suppressed residual interaction using a parity-violated superconducting qubit,” arXiv:2005.02630 (2020).
- [45] David C. McKay, Sarah Sheldon, John A. Smolin, Jerry M. Chow, and Jay M. Gambetta, “Three-Qubit Randomized Benchmarking,” *Physical Review Letters* **122**, 200502 (2019).
- [46] A. D. Córcoles, Jay M. Gambetta, Jerry M. Chow, John A. Smolin, Matthew Ware, Joel Strand, B. L.T. Plourde, and M. Steffen, “Process verification of two-qubit quantum gates by randomized benchmarking,” *Physical Review A - Atomic, Molecular, and Optical Physics* **87**, 030301 (2013).
- [47] Uri Vool and Michel Devoret, “Introduction to quantum electromagnetic circuits,” *International Journal of Circuit Theory and Applications* **45**, 897–934 (2017).
- [48] J. A. Schreier, A. A. Houck, Jens Koch, D. I. Schuster, B. R. Johnson, J. M. Chow, J. M. Gambetta, J. Majer, L. Frunzio, M. H. Devoret, S. M. Girvin, and R. J. Schoelkopf, “Suppressing charge noise decoherence in superconducting charge qubits,” *Physical Review B - Condensed Matter and Materials Physics* **77**, 180502 (2008).
- [49] D. I. Schuster, A. Wallraff, A. Blais, L. Frunzio, R. S. Huang, J. Majer, S. M. Girvin, and R. J. Schoelkopf, “Ac Stark shift and dephasing of a superconducting qubit strongly coupled to a cavity field,” *Physical Review Letters* **94**, 123602 (2005).
- [50] C Macklin, D Hover, M E Schwartz, X Zhang, W D Oliver, and I Siddiqi, “A near – quantum-limited Josephson traveling-wave parametric amplifier,” *Science* **350**, 307 (2015).
- [51] David C. McKay, Christopher J. Wood, Sarah Sheldon, Jerry M. Chow, and Jay M. Gambetta, “Efficient Z gates for quantum computing,” *Physical Review A* **96**, 022330 (2017).
- [52] Tanay Roy, Sumeru Hazra, Suman Kundu, Madhavi Chand, Meghan P. Patankar, and R. Vijay, “Programmable Superconducting Processor with Native Three-Qubit Gates,” *Physical Review Applied* **14**, 014072 (2020).
- [53] Michael A. Nielsen and Isaac L. Chuang, *Quantum Computation and Quantum Information* (2010).
- [54] Easwar Magesan, Jay M. Gambetta, and Joseph Emerson, “Characterizing quantum gates via randomized benchmarking,” *Physical Review A - Atomic, Molecular, and Optical Physics* **85**, 042311 (2012).
- [55] J. Kelly, R. Barends, B. Campbell, Y. Chen, Z. Chen, B. Chiaro, A. Dunsworth, A. G. Fowler, I. C. Hoi, E. Jeffrey, A. Megrant, J. Mutus, C. Neill, P. J.J. O’Malley, C. Quintana, P. Roushan, D. Sank, A. Vainsencher, J. Wenner, T. C. White, A. N. Cleland, and John M. Martinis, “Optimal quantum control using randomized benchmarking,” *Physical Review Letters* **112**, 240504 (2014).
- [56] Nikolaus Hansen, Youhei Akimoto, and Petr Baudis, “CMA-ES/pycma on Github,” Zenodo, DOI:10.5281/zenodo.2559634 (2019).
- [57] Sarah Sheldon, Lev S. Bishop, Easwar Magesan, Stefan Filipp, Jerry M. Chow, and Jay M. Gambetta, “Characterizing errors on qubit operations via iterative randomized benchmarking,” *Physical Review A* **93**, 12301 (2016).
- [58] Z. Wang, S. Shankar, Z. K. Mineev, P. Campagne-Ibarcq, A. Narla, and M. H. Devoret, “Cavity Attenuators for Superconducting Qubits,” *Physical Review Applied* **11**, 014031 (2019).
- [59] Fei Yan, Dan Campbell, Philip Krantz, Morten Kjaergaard, David Kim, Jonilyn L. Yoder, David Hover, Adam Sears, Andrew J. Kerman, Terry P. Orlando, Simon Gustavsson, and William D. Oliver, “Distinguishing Coherent and Thermal Photon Noise in a Circuit Quantum Electrodynamical System,” *Physical Review Letters* **120**, 260504 (2018).
- [60] Jay M. Gambetta, A. D. Córcoles, S. T. Merkel, B. R. Johnson, John A. Smolin, Jerry M. Chow, Colm A. Ryan, Chad Rigetti, S. Poletto, Thomas A. Ohki, Mark B. Ketchen, and M. Steffen, “Characterization of addressability by simultaneous randomized benchmarking,” *Physical Review Letters* **109**, 240504 (2012).
- [61] Vinay Tripathi, Mostafa Khezri, and Alexander N. Korotkov, “Operation and intrinsic error budget of a two-qubit cross-resonance gate,” *Physical Review A* **100**, 012301 (2019).
- [62] S. Filipp, P. Maurer, P. J. Leek, M. Baur, R. Bianchetti, J. M. Fink, M. Göppl, L. Steffen, J. M. Gambetta, A. Blais, and A. Wallraff, “Two-qubit state tomography using a joint dispersive readout,” *Physical Review Letters* **102**, 200402 (2009).
- [63] Guanyu Zhu, David G. Ferguson, Vladimir E. Manucharyan, and Jens Koch, “Circuit QED with fluxonium qubits: Theory of the dispersive regime,” *Physical Review B - Condensed Matter and Materials Physics* **87**, 24510 (2013).
- [64] Maxime Boissonneault, J. M. Gambetta, and Alexandre Blais, “Dispersive regime of circuit QED: Photon-dependent qubit dephasing and relaxation rates,” *Physical Review A - Atomic, Molecular, and Optical Physics* **79**, 13819 (2009).
- [65] D. H. Slichter, R. Vijay, S. J. Weber, S. Boutin, M. Boissonneault, J. M. Gambetta, A. Blais, and I. Siddiqi, “Measurement-induced qubit state mixing in circuit QED from Up-converted dephasing noise,” *Physical Review Letters* **109**, 153601 (2012).
- [66] Daniel Sank, Zijun Chen, Mostafa Khezri, J. Kelly, R. Barends, B. Campbell, Y. Chen, B. Chiaro,

- A. Dunsworth, A. Fowler, E. Jeffrey, E. Lucero, A. Megrant, J. Mutus, M. Neeley, C. Neill, P. J.J. O'Malley, C. Quintana, P. Roushan, A. Vainsencher, T. White, J. Wenner, Alexander N. Korotkov, and John M. Martinis, "Measurement-Induced State Transitions in a Superconducting Qubit: Beyond the Rotating Wave Approximation," *Physical Review Letters* **117**, 190503 (2016).
- [67] Daria Gusenkova, Martin Spiecker, Richard Gebauer, Madita Willsch, Francesco Valenti, Nick Karcher, Lukas Grünhaupt, Ivan Takmakov, Patrick Winkel, Dennis Rieger, Alexey V. Ustinov, Nicolas Roch, Wolfgang Wernsdorfer, Kristel Michielsen, Oliver Sander, and Ioan M. Pop, "Quantum non-demolition dispersive readout of a superconducting artificial atom using large photon numbers," arXiv:2009.14785 (2020).
- [68] U. Vool, I. M. Pop, K. Sliwa, B. Abdo, C. Wang, T. Brecht, Y. Y. Gao, S. Shankar, M. Hatridge, G. Catelani, M. Mirrahimi, L. Frunzio, R. J. Schoelkopf, L. I. Glazman, and M. H. Devoret, "Non-poissonian quantum jumps of a fluxonium qubit due to quasiparticle excitations," *Physical Review Letters* **113**, 247001 (2014).
- [69] Vladimir E Manucharyan, *Superinductance*, Ph.D. thesis (2012).
- [70] Easwar Magesan, Jay M. Gambetta, B. R. Johnson, Colm A. Ryan, Jerry M. Chow, Seth T. Merkel, Marcus P. Da Silva, George A. Keefe, Mary B. Rothwell, Thomas A. Ohki, Mark B. Ketchen, and M. Steffen, "Efficient measurement of quantum gate error by interleaved randomized benchmarking," *Physical Review Letters* **109**, 080505 (2012).
- [71] Joel J. Wallman, "Randomized benchmarking with gate-dependent noise," *Quantum* **2**, 47 (2018).
- [72] Line Hjortshøj Pedersen, Niels Martin Møller, and Klaus Mølmer, "Fidelity of quantum operations," *Physics Letters, Section A: General, Atomic and Solid State Physics* **367**, 47–51 (2007).
- [73] J. M. Chow, J. M. Gambetta, L. Tornberg, Jens Koch, Lev S. Bishop, A. A. Houck, B. R. Johnson, L. Frunzio, S. M. Girvin, and R. J. Schoelkopf, "Randomized benchmarking and process tomography for gate errors in a solid-state qubit," *Physical Review Letters* **102**, 090502 (2009).